ABSTRACT

Title of Document:	SIMULATION OF DUAL-MODE SCRAMJET UNDER THERMALLY CHOKED VS. SUPERSONIC COMBUSTION MODE
Degree Candidate:	Cameron Westley Butcher Master of Science, 2014
Directed By:	Associate Professor Kenneth H. Yu Department of Aerospace Engineering

Effects of combustion mode and cavity flame-holder on dual-mode scramjet performance were investigated using a two-dimensional computational framework developed from commercial finite element software. The objectives were to simulate the experimental data from a laboratory model scramjet with mixing enhancement device, provide better understanding of the physical processes, and to analyze the quantitative effects on the potential performance. The isolator flow field was modeled separately to match the experimentally obtained pressure rise during the Mach 2.1 isolator entry condition. The combustor heat release distribution was systematically adjusted to reproduce the wall pressure distributions from the experiments. Case studies were conducted with and without the presence of the wall cavity for scramjet operation under both thermally-choked and supersonic-combustion mode. The combustion mode affected potential tradeoffs between thrust increase and higher thermal protection need.

The presence of the cavity dampened the extent of the tradeoffs by reducing the temperature change.

SIMULATION OF DUAL-MODE SCRAMJET UNDER THERMALLY
CHOKED VS. SUPERSONIC COMBUSTION MODE

By

Cameron Westley Butcher

Thesis submitted to the Faculty of the Graduate School of the
University of Maryland, College Park, in partial fulfillment
of the requirements for the degree of
Master of Science
2014

Advisory Committee:
  Professor Kenneth Yu, Chair
  Professor James Baeder
  Professor Christopher Cadou

Dedication

To my fiancée Lindsay and my parents Dan and Sandi. I truly thank you for your support and for helping me accomplish this goal. It wouldn't have been possible without you. I would also like to dedicate this work to my uncle, without whom I never would have been so interested in the aerospace field. Thank you.

Acknowledgements

I would like to thank my advisor, Dr. Yu, for all of his support, thoughts, and direction in completing this research. His guidance helped in each step of this process. I would also like to thank my committee members, Dr. Baeder and Dr. Cadou, as their instruction proved vital for this work. In addition, I thank my fellow researchers working under Dr. Yu, Dr. Laurence, and Dr. Lewis for their input and ideas. This work would not have been possible without the assistance and willingness to allow the use of the experimental results that were gathered by Dr. Camilo Aguilera during his PhD studies at this university.

Finally, I gratefully acknowledge the support of the U.S. Air Force Office of Scientific Research with Dr. Michael Kendra as Program Manager, through the University of Maryland Center for Revitalization of the Hypersonic Testing and Evaluation Workforce program.

Table of Contents

List of Tables

List of Figures

viii

Nomenclature

Letters, Symbols, and Abbreviations

a	= Local speed of sound
A	= Area
c_p	= Specific heat capacity at constant pressure
f	= Fuel – air ratio ($f = \dot{m}_{fuel}/\dot{m}_{air}$)
H	= Height of isolator (0.5 *in*)
h_{pr}	= Heat of reaction (also known as enthalpy of combustion)
M	= Mach number
$\dot{m}$	= Mass flow rate
P	= Pressure
P_o	= Stagnation pressure at isolator entrance for each case
Q	= Amount of heat release per unit depth in 2-D simulations (*W/m*)
R_s	= Specific gas constant
u	= X-component of velocity
w_f	= Width of fuel injection slot
x	= x – location (*in*); For scramjet models, $x = 0$ is point where isolator meets the combustor
β	= Parameter used in calculation for c_p of H$_2$ fuel (Appendix A2)
γ	= Ratio of specific heats
η_c	= Combustion/Mixing Efficiency
Φ	= Combustor equivalence ratio
ρ	= Density
τ	= Thrust
θ	= Inlet boundary layer momentum thickness or deflection angle, depending on context
ϑ	= Empirical constant that depends on rate of mixing

Subscripts

$2D, 3D$	= Parameter value in 2- or 3-D space, respectively
Cav	= Cavity
def	= Deflection angle of bottom surface of scramjet internal flow path
f	= Fuel
HR	= Heat release
in	= Inlet
inj	= Injection
o	= Total conditions
out	= Outlet/Exit
st	= Stoichiometric

Acronyms

CFD	=	Computational Fluid Dynamics
DARPA	=	Defense Advanced Research Projects Agency
DNS	=	Direct Numerical Simulation
HMNF	=	High Mach Number Flow
LES	=	Large Eddy Simulation
LHV	=	Lower Heating Value (of fuel)
MATLAB	=	Matrix Laboratory
NASA	=	National Aeronautics and Space Administration
RANS	=	Reynolds-averaged Navier-Stokes
STP	=	Standard Temperature and Pressure (273.15 K, 1 atm)

Chapter 1: Introduction

1.1. Background and Motivation

Scramjet engines are of particular interest for single-stage-to-orbit launch vehicles, hypersonic transport aircraft, or munitions delivery systems. Dual-mode scramjet engines are capable of being run at a much wider wide range of operating conditions than a dedicated ramjet or scramjet on its own. They contain complex internal flow fields such as that which was seen during the experiments that were conducted by *Aguilera* [1]. In order to better understand the flow field within and the effect of each part of the geometry on the performance of the engine, it is desired to set up a computational framework in which the engine can be analyzed in more detail over a wider range of conditions.

There are several aspects of dual-mode scramjets that are of particular interest. Thermal choking is of concern in the case of many experimental scramjet rigs such as those of *Aguilera* [1] and *Fotia and Driscoll* [2]. If not controlled properly, thermal choking can eventually lead to inlet unstart if the high backpressure is allowed to propagate upstream and be disgorged by the inlet. In this situation, the performance of the engine is greatly reduced by increasing drag, reducing the amount of mass flow that can pass through the engine, and producing lower thrust [3,4].

Other aspects of interest are to gain more insight into the effect of transverse fuel injection into a supersonic cross-flow and the effect of a cavity flame holder on

1

the pressure data along the top wall of the combustor. Figure 1.1 shows experimental

pressure results for a range of equivalence ratio values.
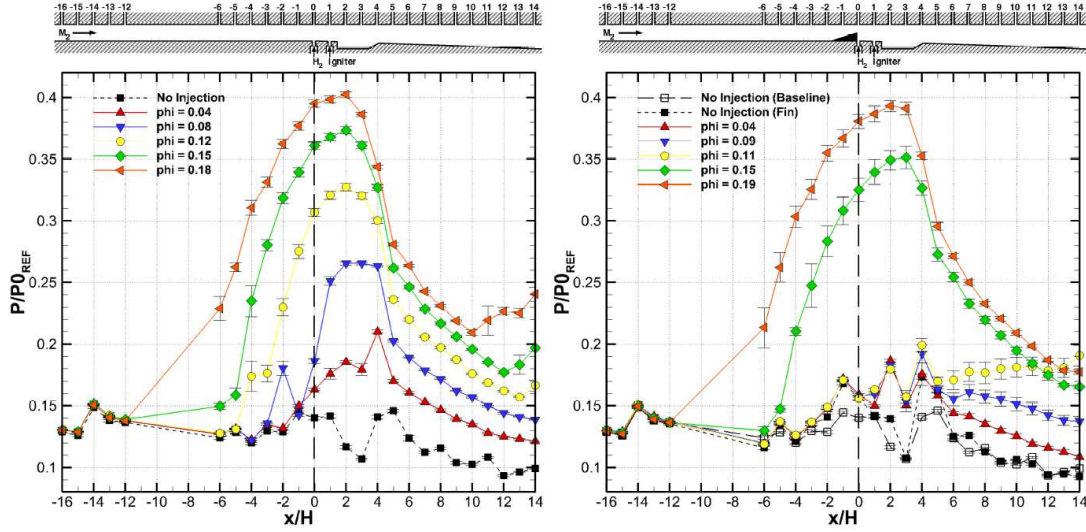
Figure 1.1: Experimental pressure data along top wall for baseline (*left*) and fin-guided (*right*) cases. *Reproduced with permission from the author* [1].

When analyzing the results shown in the above figure, one particular run stands out against

the others – the fin-guided case of $\Phi = 0.11$. In all other cases, the general trend is a decrease

in pressure downstream of $x/H = 4$ whether the run was thermally choked or not. However,

for this particular set of results, the pressure increases. This leads to believe that the effect of

heat addition is great enough to overcome the area expansion, but not so great as to cause the

flow to become choked as with the higher equivalence ratios. This is one of the first times that

this behavior has been seen in experiments so it is of great interest to try to support this theory

with a simulation. Results shown by *Fotia and Driscoll* in multiple papers [5,6] show the

pressure always decreasing.

This leads to another area of particular interest: the effect of heat release location and

intensity on the overall flow field. Due to limitations for the model scramjet setup, optical

access is restricted to a small region of the combustor. For the fin-guided cases, it was shown

that the heat release was spread out over a much larger region that extended downstream of the

2

visible region. This can be seen in [1]. By extrapolating the data that is available, an estimated combustion zone can be found and modeled.

1.2. Technical Objectives

The work presented herein used a commercially available physics-based simulation software package to model the internal flow field of a dual-mode scramjet. The model scramjet was part of the Hypersonic Research Center at the University of Maryland College Park. The goal was to create a framework with which a variety of different simulations could be run and compared with static pressure and OH[*] chemiluminescence data presented by *Aguilera* [1]. The specific objectives for this research were:

1.) Set up computational framework using COMSOL Multiphysics 4.4 to simulate the internal flow field of a dual-mode scramjet.

   a. Test the feasibility of using COMSOL for modeling said flow field.

   b. Validate framework using experimental data.

   c. Generate flow features seen in experiments [1] including isolator shock trains, fuel injection induced shock wave, and thermal choking over a range of combustor equivalence ratios.

2.) Quantitatively deduce spatial distribution of heat release characteristics obtained in experiments.

   a. Show individual effect of cavity and fuel injection in combustor.

   b. Analyze thermally choked and supersonic heat release profiles.

   c. Create simplified combustor model to show effect of heat addition and area expansion only.

3

d. Vary the heat release in streamwise and wall-normal directions and analyze the resulting flow field.

e. Vary heat release intensity and analyze point at which flow is thermally choked.

3.) Analyze basic engine performance parameters such as thrust and maximum wall temperature under various modes of operation to quantitatively infer the effect of the cavity on performance.

a. Quantify the drag penalty caused by the presence of a cavity.

b. Learn the effect of the cavity on the maximum wall temperature of the flow and compare for different modes of operation.

By analyzing the heat release pattern in detail as outlined above, more information can be learned about the complex flow field contained within the model scramjet. The effects of area expansion and heat addition can be compared to experimental pressure data to find the point at which the effects of heat addition outweigh the expansion without causing the flow to be thermally choked. Finally, basic engine performance properties can be quantitatively deduced from the simulated results for non-reacting, supersonic, and thermally choked conditions.

1.3. Scope of Present Work

The main focus of the current work is two-fold: to prove the feasibility of using COMSOL Multiphysics to model the internal flow field of a hypersonic airbreathing engine, and to compare performance characteristics under several different modes of operation. Due to the limitations in computational power of using a single machine, the model scramjet was modeled in two-dimensional space using a stationary time study.

Several simplifications and assumptions were made from the original work by *Aguilera* [1]. After developing the computational framework, several cases will be analyzed and compared to quantitatively learn the effect of geometry and combustion mode.

The sections that follow will present a synopsis of the current research trends involving the flow features that were focused on for the purpose of this research in Chapter 2, a brief overview of the commercial software package that was used in Chapter 3, and a breakdown of the problem set up and results in Chapters 4-5. Chapter 6 presents some conclusions and remarks, followed by several appendices that present simulation run time data, additional simulation results, and any derivations that were performed.

Chapter 2: Literature Review

2.1. Dual-mode Scramjet

2.1.1. Introduction

Scramjet engines have long been the focus of research for those interested in hypersonic flight regimes for military applications and space launch vehicles including but not limited to single-stage- or two-stage-to-orbit launch vehicles, such as the National Aerospace Plane Program of the 1980s and 1990s [3,7]. However, their actual in-flight testing has been limited in scope. In the United States, NASA is one of the leading agencies that continues conducting research in scramjet propulsion. However, DARPA was heavily involved with the National Aerospace Plane Program during the program's existence [7]. Several other countries have conducted research with scramjet engines to varying extents including, but not limited to: Russia, France, Germany, Japan, and Australia. For a brief history on the developments of scramjet engines since the 1960s, see the work by *Curran* [7].

Dual-mode scramjets in particular are known to have a much wider range of flight regimes than a ramjet or scramjet engine alone. A ramjet is only efficient to a maximum speed of around Mach 5, but a dual-mode scramjet can operate in the range of Mach 3 to 20 with little to no change in geometry [3]. In laboratory settings, especially at universities, dual-mode scramjets are commonly used for scramjet testing due to their wide operating ranges and ability to support supersonic combustion at lower Mach numbers. Examples of these have been presented by *Aguilera* [1], *Le et al.*

[3], *Goyne et al.* [8], and others. One of the most prominent currently active university-based scramjet research programs at the time of this writing is at the University of Michigan. Several of their latest papers will be discussed throughout this chapter.

2.1.2. Isolator

Dual-mode scramjet engines contain a defined isolator section as part of their geometry. The purpose of the isolator is exactly as the name implies – to shield the inlet from the effects caused by the combustor such as pressure rise. In addition, dual-mode scramjets have a much wider operating range than a pure ramjet or scramjet engine [3]. This is very advantageous for the idea of a single-stage-to-orbit launch vehicle that would need to operate at a very wide range of flight Mach numbers throughout its trajectory.

The scramjet isolator has been studied analytically, experimentally, and computationally by a wide range of researchers around the world. Some examples of research in the physics governing the flow field and the theory, modeling, or experimentation of said flows were performed by *Le et al.* [3], *Smart* [9], *Geerts and Yu* [10], *Matsuo et al.* [11], *Morgan et al.* [12], *Sun et al.* [13], and *Tan et al.* [14].

In one particular study, *Le et al.* showed that the addition of an isolator was able to drastically improve the range of combustor equivalence ratio values over which the scramjet could be operated [3]. The addition of the isolator also proved beneficial in retaining some control over the shock train location.

7

2.2. Isolator Shock Train

2.2.1. Introduction

It is typical to encounter a shock train in a dual-mode scramjet isolator. This shock train serves the purpose of allowing the inlet pressure to remain the same while allowing the pressure to rise to match that from the combustion [4]. In cases where the isolator exceeds the maximum allowable static pressure rise, the shock train will propagate upstream and be disgorged by the inlet in a condition known as inlet unstart [3,4]. The maximum allowable static pressure rise is a function of the length of the isolator and the inlet conditions. It can be calculated using the following relationship [4].

$$\frac{L(M_1^2 - 1)Re_\theta^{1/4}}{H\sqrt{\theta/H}} = \left[50\left(\frac{P_2}{P_1} - 1\right) + 170\left(\frac{P_2}{P_1} - 1\right)^2\right] \qquad (2.1)$$

Similarly, equation (2.1) can be used to estimate the required isolator length if given the pressure rise that is to be expected.

The structure of the shock train is dependent on both the back pressure ratio and the boundary layer. As the pressure downstream of the combustor is increased, the flow upstream must adjust to the new conditions. It does this by generating a shock train

2.2.2. Previous Studies

Many isolator shock train studies have been completed by a wide range of authors. One particular study presented by *Fotia and Driscoll* [5] looked into the coupling between the combustor and isolator in a dual-mode scramjet engine and proposed a new way of representing this behavior. They broke the traditional way of

8

expressing the thermal choking, or flow blockage, into two distinct new representations. The isolator back pressure caused from downstream combustion can now be thought of as a chemical blockage, while fuel injection can be represented as a mechanical blockage. By decoupling these two effects, the authors were able to analyze each one in more detail and derive a model for analyzing the shock train properties [5].

2.3. Heat Release and Thermal Choking

2.3.1. Introduction

Thermal choking is an extremely undesirable condition for a scramjet engine. Ramjets are designed to thermally choke in order to decrease the flow velocity inside the combustor. However, once the flow gets above a Mach number of 5-7, depending on the source, the losses that are encountered to decelerate a flow from such a high velocity overpower the benefits of subsonic combustion.

A simple calculation shown by *Le et al.* can be performed to estimate the pressure ratio for an isolator-combustor combination at which the flow will thermally choke. Because the heat release typically occurs over a large area, it is assumed that there is uniform heat addition and that the gas is calorically perfect [3].

$$\frac{P_3}{P_1} = \frac{1 + \gamma M_1^2}{1 + \gamma M_3^2} \tag{2.2}$$

By setting the final Mach number to 1, the pressure ratio at which the flow will begin to thermally choke is given by equation (2.2) [3].

2.3.2. Area Divergence

The most common method many dual mode scramjet engines use to help delay the onset of thermal choking is to have a slight area divergence in the combustor. This method is employed in both experimental [1,5,6,8] and numerical models [2,15]. Typically, the divergence ranges between 2 *degrees* [1] and 4 *degrees* [5].

2.3.3. Combustion Modeling

Combustion can be modeled in a number of ways, ranging from 1-D simplified models all the way up to full 3-D chemically reacting LES or DNS. A very simple 1-D heat release model is presented by *Smart* [9]. This model expands on the work presented by *Heiser and Pratt* [4]. While the work by *Smart* primarily focuses on scramjet isolators, he presents a simple model that uses two algebraic equations to predict the heat release curve for a given chemical reaction. This model takes into account the fuel injection location, combustor length, and estimated combustion efficiency [9]. Once all of the required parameters have been substituted into the equations, it reduces to a function of the local x-coordinate as the flow marches downstream through the combustor.

$$\eta_c = \eta_{c,tot} \left[\frac{\vartheta X}{1 + (\vartheta - 1)X} \right] \qquad (2.3)$$

Where
$$X = \frac{x - x_3}{x_4 - x_3}$$

The subscripts in the equation above represent the fuel injector location (*3*) and end of combustor (*4*) in a reference frame where the combustor starts at $x_2 = 0$. This is used to generate data for the stagnation temperature rise through the combustor taking into account heat loss to the structure, dQ [9].

10

$$T_o = T_{o_2} + (h_{pr}f_{st}\phi\eta_c - dQ)/c_p \qquad (2.4)$$

Supersonic combustion is an extremely transient and turbulent process. These oscillatory flow characteristics are difficult to capture accurately and require specialized dedicated models in order to learn more about these processes. One such model was developed by *Choi et al.* [16] that used a blend of two separate turbulence models: $k - \epsilon$ and $k - \omega$. This model had transverse fuel injection into a supersonic cross-flow upstream of a rectangular cavity in the bottom wall of the combustor. The authors determined that the effects from the cavity are more prevalent than shock wave-boundary layer interactions [16]. Flow unsteadiness causes strong pressure oscillations along the top wall in cases where the combustion occurred throughout the entire combustor geometry. In extreme cases, these oscillations have the ability to thermally choke the flow and/or cause inlet unstart [16].

Another combustion model was developed by *Berglund and Fureby* [17]. This particular model used an LES approach to simulate a one-sided diverging channel with a wedge-shaped cavity for flame holding. The authors felt that using LES gave an advantage over the use of simplified RANS models because it more accurately captures both the large and small scale turbulent flow features [17]. It is also claimed by the authors that the use of LES for supersonic reacting flow simulation had been very limited before developing their model. Two separate flamelet models, a one-equation model that neglects thermal diffusion and a two-equation model that takes it into account, were utilized to model the combustion process. Using this method, they were able to predict both the baseline and reacting flow fields and find good agreement when compared to experimental data [17].

11

2.3.4. Thermal Choking

Thermal choking is an important issue for dual-mode scramjet engines. Because they are designed with thermal choking in mind, they have to be able to withstand the increases in temperature and pressure associated with decelerating the flow from supersonic to subsonic speeds. Estimated conditions can be seen in Table 2.1.

Table 2.1: Comparison of flow properties between supersonic combustion and thermally choked modes of operation for scramjet in Mach 12 flight. Adapted from [18].

Parameter	Combustion Chamber Entrance		Combustion Chamber Exit	
	Supersonic	Thermally Choked	Supersonic	Thermally Choked
Pressure (*atm*)	2.7	75	2.7	75
Temperature (*K*)	1250	4500	2650	4200
Mach Number	4.9	0.33	3.3	0.38

Thermal protection systems must be able to protect the materials from being subjected to the extremely high temperatures that are possible as shown in Table 2.1. In most cases however, vehicles in Mach 12 flight would be operated in pure scramjet mode unless operating off-design. It is typically in ramjets and dual-mode scramjets that thermal choking is of most concern.

An analytical model for thermal choking in a two-dimensional expanding flow is derived and presented by *Delale and van Dongen* [19]. They develop a model that defines the critical heat release value that will cause a supersonic flow to thermally choke and become subsonic. The model constructs a partial differential equation that takes into account the area divergence and amount of heat that is added to the flow [19].

2.4. Flame-Holding Cavity

2.4.1. Introduction

Flame holding cavities in supersonic combustion have been studied both experimentally and numerically. Research in experiments by *Aguilera* [1], *Yu et al.* [20], *Micka and Driscoll* [21], and *Mathur et al.* [22] all used a cavity-based flame holder on the bottom wall of the combustor with fuel injection just upstream of the cavity. According to *Yu et al.*, cavities help reduce the overall combustor length by aiding in mixing, increasing the flow residence time by setting up a region of recirculating flow, and assisting in flame holding to ignite the fuel-air mixture [20]. In many cases, such as [20], [21], the combustor geometry begins to diverge at the end of the cavity to prevent thermal choking as mentioned previously.

2.4.2. Cavity Geometries

There are many different geometries that have been used in experimental dual-mode scramjet combustors. A number of possible configurations were shown by *Yu et al* [20], but it is by no means an exhaustive compilation. Several of the most common configurations are shown in Figure 2.1 below.
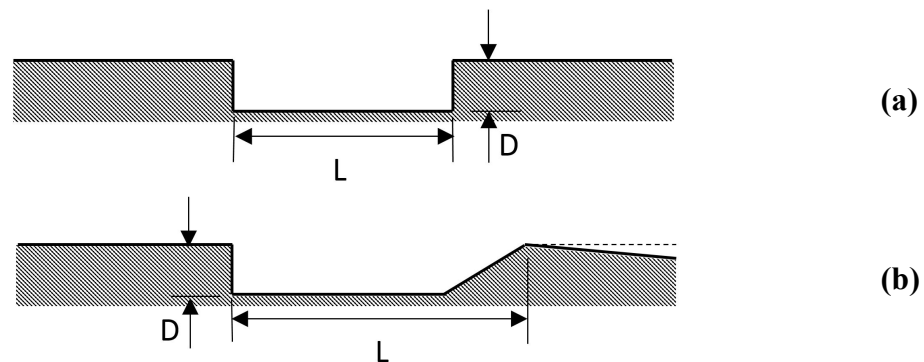
Figure 2.1: Two commonly used cavity configurations. *Adapted by author from figures in* [1,20-21].

13

Calculating the aspect ratio, or L/D, of the cavity helps determine the effect on the flow field. Low aspect ratio cavities are best for flame holding, while larger aspect ratio ones have great effect on reducing the overall flame length [20]. Shorter flame length can be beneficial if the combustor geometry is restricted to a very small overall length. The size, shape, and location of the cavity used must be found based on the design parameters and tradeoffs between mixing enhancement and drag induced by the cavity [20].

2.4.3. Effect of Cavity of Flow Field

In a study by *Micka and Driscoll*, it was found that there are two main forms of combustion stabilization for a dual-mode scramjet in ramjet mode: cavity-based, and fuel jet-wake [21]. For the cavity-based combustion stabilization method, the combustion zone is affixed at the leading edge of the shear layer caused by the cavity. Contrarily, the wake stabilization is positioned just downstream of the injection orifice in the wake caused from the fuel injection [21]. It was seen that a combination of these two modes can exist under certain conditions, causing an instability. This can be mitigated by careful design of the fuel injection location such that the pressure will not oscillate by causing the two stabilization modes to essentially overlap. When the engine operates in pure scramjet mode, the fuel jet-wake mode was not seen [21].

Cavities were also investigated numerically by *Choi et al.* [16] and *Wang et al.* [23]. They explored the effect of a cavity on flow unsteadiness and the ensuing flame evolution. A total of twelve different cases were simulated by *Choi et al.* and they were able to show the pressure fluctuations with time for both reacting and non-reacting cases, with and without a cavity, and using three different fuel injection pressures [16].

14

It is this unsteadiness that was mentioned in [21]. In another study using a hybrid RANS/LES simulation conducted by *Wang et al.* [23], the authors were able to capture and analyze two similar modes that were presented in [21]. Vortices shed by the aft wall of the cavity greatly affected the instabilities but can be weakened slightly by upstream fuel injection [23]. The authors delved deeply into the effects of the shear layer caused by the cavity and how it affected the cross-flow above. Similar to the results presented in [16], they showed pressure oscillations as a function of time. Figure 2.1 shows some of the simulation results that were presented by *Wang et al.* [23].
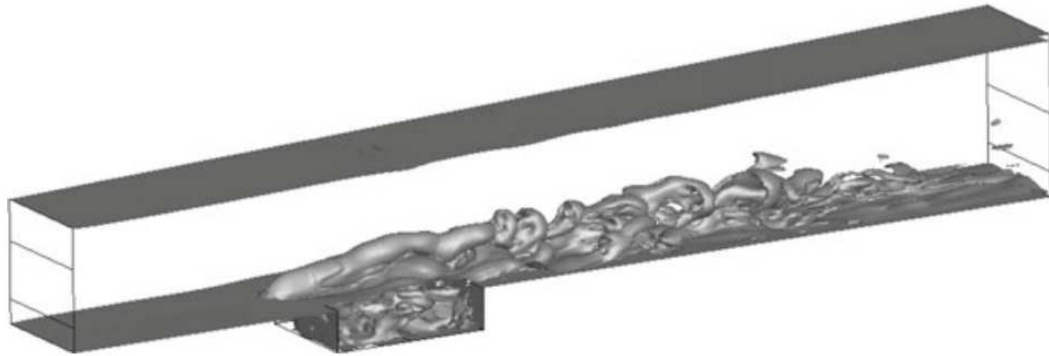
Figure 2.2: Hybrid RANS/LES simulation showing fuel injection just upstream of cavity with vortices being shed off of the aft wall and being transported downstream. *Adapted by author from* [23].

15

Chapter 3: Introduction to COMSOL Multiphysics

3.1. Introduction

COMSOL, Inc. is a Swedish based company that was founded in 1986 by Svante Littmarck and Farhad Saeidi [24]. The first version of COMSOL Multiphysics, a finite element-based software package, was released in 1998 and has since grown to include add-on modules for many branches of physics such as structural mechanics, fluid flow, AC/DC, and electromagnetics [24,25]. As of the current COMSOL Multiphysics 5.0 release, there are a total of forty-one add-on products and modules for added physics capabilities, CAD geometry import, and a suite of LiveLink products that interface with MATLAB, SOLIDWORKS, Microsoft Excel, and more. One of the key functionalities of COMSOL is the ability to couple multiple physics together when simulating a real-world system. Rather than needing several different programs to model the system properly, it can all be coupled together and solved in conjunction with one another. Sets of PDEs are solved simultaneously and permit the calculation of temperature fluxes and time rate of change of variables to allow for a more realistic solution.

The COMSOL Multiphysics base package contains all of the tools necessary to set up a simulation with limited physics capabilities. The basic tools for creating geometry are found in the base package, but file import is not supported for most CAD file types without the *CAD Import Module*. Some physics capabilities are present, but only on a very limited basis, as most of them are found in the add-on modules instead.

16

All of the meshing tools, solvers, postprocessing, and analysis tools are found in the base package. Users have the ability to solve more physics-intensive problems without the add-on modules, but they must manually add all of the equations that are required to solve their problem of interest.

3.2. Modeling Process

The process for setting up a model in COMSOL is a straightforward procedure that is similar regardless of the physics of interest. The easiest way to set up a new simulation is to use the *Model Wizard* feature. This wizard walks the user through the process of selecting the geometry space dimension, adding the physics, and selecting the type of study to run. After completing the necessary parts of the wizard, the user is taken to the COMSOL work environment. It contains several main features:

- The model tree (far left) shows all of the steps that have been taken to set up the model. Each main category has its own branch such as geometry, physics, and mesh. Located below each branch are nodes that show the shapes that were used to create the geometry, boundaries or operations that were added to the physics, and the mesh control properties.

- The settings window (left center) is where the dimensions, variables, or expressions are entered for the node that is selected in the model tree. This is also where the settings are changed for the physics, boundary conditions, or other branches or nodes.

- The graphics window (upper right) is where the user can visualize the geometry, results, or convergence plots. As with most plotting tools, there is functionality to pan, zoom, or rotate a 3-D object.

17

- The message and progress window (lower right) is where the user receives messages from the software such as number of mesh elements, degrees of freedom that were solved for, and the solution time. The progress window shows how far along the study is during solving.

- The ribbon (top) allows the user to easily select items to add to the model tree. Each main branch has its own tab on the ribbon that contains the related features that are needed to build the model. For example, the physics tab contains boundary conditions, constraints, and the ability to couple to other physics that have been added to the model. Most all of the features that are found in the ribbon can also be added by right clicking on the appropriate node or branch in the model tree, but the ribbon provides a more user-friendly method to locate items. Most people that are familiar with the Microsoft Office suite of products released after 2003 will find the ribbon very intuitive to use.

Independent of the type of problem being solved, the procedure is always as follows: geometry, physics, mesh, solve, and then postprocessing the results. If the user follows the model tree from top to bottom, these are the main nodes that they will encounter, respectively. Much more detailed information and procedures can be found in [25]. For information on a particular module, see the documentation that is included with the module itself.

3.3. Physics of Interest

For the purpose of this research, the main topic of interest is the internal flow field inside the dual-mode scramjet engine. Due to the high Mach number found inside a

scramjet engine, the *High Mach Number Flow* portion of the *CFD Module* were used in COMSOL Multiphysics 4.4.

3.3.1. High Mach Number Flow

This particular physics, with the COMSOL identifier "hmnf," is intended for compressible flows in which the Mach number is above 0.3. It solves the fully compressible Navier-Stokes equations that govern the fluid flow. These are found in [26, 27]. The Navier-Stokes equations are a set of three individual equations derived using the conservation of mass, momentum, and energy. The conservation of mass, or continuity equation, is as follows:

$$\frac{\partial \rho}{\partial t} + \nabla \cdot (\rho \boldsymbol{u}) = 0 \qquad (3.1)$$

where bold quantities represent vectors in all equations. Equation (3.1) states that mass can neither be created nor destroyed: it must remain constant for a given control volume [27]. The second Navier-Stokes equation is derived from the conservation of momentum.

$$\rho \frac{\partial \boldsymbol{u}}{\partial t} + \rho (\boldsymbol{u} \cdot \nabla) \boldsymbol{u} = \nabla \cdot [-p\boldsymbol{I} + \tau] + \boldsymbol{F} \qquad (3.2)$$

Equation (3.2) states that the time rate of change of momentum must be equivalent to the force exerted on the body [27]. The body force terms are on the right side of the equation. The third and final equation is derived using the conservation of energy.

$$\rho C_p \left(\frac{\partial T}{\partial t} + (\boldsymbol{u} \cdot \nabla) T \right) = -(\nabla \cdot \boldsymbol{q}) + \tau : \boldsymbol{S} - \frac{T}{\rho} \frac{\partial \rho}{\partial T} \bigg|_p \left(\frac{\partial p}{\partial t} + (\boldsymbol{u} \cdot \nabla) p \right) + Q \qquad (3.3)$$

Where τ is the viscous stress tensor, $\boldsymbol{q}$ is the heat flux vector, Q is the heat source over a volumetric domain, and $\boldsymbol{S}$ is defined as [26]

19

$$S = \frac{1}{2}(\nabla \boldsymbol{u} + (\nabla \boldsymbol{u})^T)$$

Equation (3.3) states that energy must remain constant. It can change form, but it cannot be created nor destroyed [27].

3.3.2. Turbulence Models

The *High Mach Number Flow* module contains two built-in turbulence models: $k - \epsilon$ and *Spalart-Allmaras*. While each model can be found under a separate node in the *Add Physics* menu, it is easy to change from one model to the other using a simple drop-down box under the *High Mach Number Flow* branch of the model tree. Rather than solving the full compressible Navier-Stokes equations, these simplified turbulence models utilize a RANS model. In order to help reduce the number of mesh elements needed to solve turbulent flow problems, the flow is divided into two main categories: large scale features that can be fully resolved and small, unresolved structures that are modeled using a less computationally expensive turbulence model:

$$\phi = \bar{\phi} + \phi' \tag{3.4}$$

where equation (3.4) represents the average and fluctuating components, respectively, of a scalar flow quantity. However, for compressible flows, equation (3.4) is written as

$$\overline{\rho' u'} \tag{3.5}$$

This still represents the same average and fluctuating components, just written using different notation. Using a technique known as Favre averaging, equations (3.4) and (3.5) can be written in terms of a density-based average [26].

$$\widetilde{u_\iota} = \frac{1}{\bar{\rho}} \lim_{T \to \infty} \frac{1}{T} \int\limits_t^{t+T} \rho(\boldsymbol{x}, \tau) u_i(\boldsymbol{x}, \tau) d\tau \tag{3.6}$$

20

$$\bar{\rho}\widetilde{u_\iota} = \overline{\rho u_\iota} \tag{3.7}$$

$$u_i = \widetilde{u_\iota} + u_i'' \tag{3.8}$$

Substituting equations (3.7) and (3.8) into equations (3.2) and (3.3),

$$\frac{\partial\bar{\rho}}{\partial t} + \frac{\partial}{\partial x_i}(\bar{\rho}\widetilde{u_\iota}) = 0 \tag{3.9}$$

$$\bar{\rho}\frac{\partial\widetilde{u_\iota}}{\partial t} + \bar{\rho}\widetilde{u_j}\frac{\partial\widetilde{u_\iota}}{\partial x_j} = -\frac{\partial\bar{p}}{\partial x_i} +$$

$$\frac{\partial}{\partial x_j}\left(\mu\left(\frac{\partial\widetilde{u_\iota}}{\partial x_j} + \frac{\partial\widetilde{u_j}}{\partial x_i}\right) - \frac{2}{3}\mu\frac{\partial\widetilde{u_k}}{\partial x_k}\delta_{ij} - \overline{\rho u_j'' u_\iota''}\right) + \overline{F_\iota} \tag{3.10}$$

Where

$$-\overline{\rho u_j'' u_\iota''} = \mu_T\left(\frac{\partial\widetilde{u_\iota}}{\partial x_j} + \frac{\partial\widetilde{u_j}}{\partial x_i}\right) - \frac{2}{3}\left(\mu_T\frac{\partial\widetilde{u_k}}{\partial x_k} + \overline{\rho_k}\right)\delta_{ij} \tag{3.11}$$

For more details about the general turbulent flow theory, see Ref. [26].

3.3.2.1. $k - \epsilon$ Model

This particular turbulence model is one of the more widely used turbulence models in existence. In addition to the equations shown previously, this model adds two additional transport equations that can be found in [26]. This model has several assumptions and limitations that must be taken into account when choosing turbulence models. First, this model assumes that the Reynolds number is relatively high [26]. While this is a vague statement, it should not be an issue for any high Mach number flows such as those modeled herein. In addition, this model assumes that production and dissipation are equal in the boundary layer so that the turbulent structures are in equilibrium [26]. While these assumptions do not hold for all cases, this model can at least serve as a first approximation. If the turbulent structures must be resolved in extremely high accuracy, then a technique such as DNS or LES might be more suitable.

21

Those methods are much more accurate, but can require orders of magnitude more computational power.

One major disadvantage of the $k - \epsilon$ model is that the assumptions made to derive the model are not valid near the wall. In order to overcome this issue and to keep computational cost as low as possible, COMSOL implements a wall boundary condition denoted *wall functions*. Rather than resolving the flow all of the way to the wall, it instead only solves to the point at which the logarithmic and viscous sublayer meet [26]. This is denoted as δ_w and can be seen in Figure 3.1.
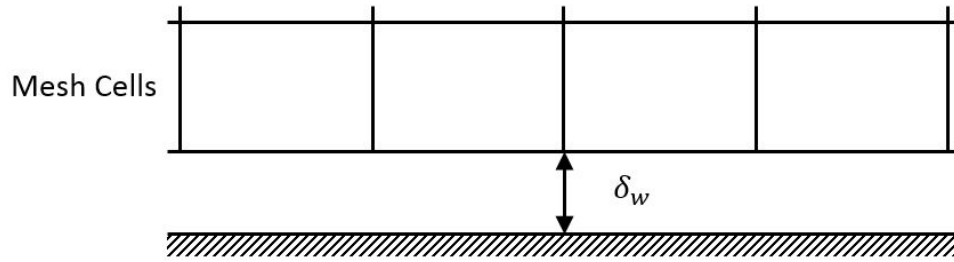
Figure 3.1: The wall functions boundary condition places the computational domain a distance away from the wall, denoted δ_w. *Diagram adapted by author from* [26].

The *wall functions* are analytical expressions that are used to estimate the flow properties in the region near the wall without the extremely fine mesh that would be required otherwise [26]. The wall lift-off, or δ_w, can also be written in terms of viscous units as:

$$\delta_w^+ = \rho u_\tau \delta_w / \mu \tag{3.12}$$

where u_τ, the friction velocity, is defined as

$$u_\tau = C_\mu^{1/4} \sqrt{k}$$

In the above equation, C_μ is an experimentally derived constant and k is the turbulence kinetic energy term, a function of turbulence variables. More detailed information can

22

be found in [26, 28]. If the mesh is sufficiently fine enough to solve the flow field, the wall lift-off will be equal to 11.06 [26]. If the mesh is too coarse, this value will become larger, dependent on how poor the mesh is. If desired, the wall roughness can be defined for many physics options that use the $k - \epsilon$ turbulence model.

3.3.2.2. Spalart-Allmaras Model

The Spalart-Allmaras turbulence model was developed by P.R. Spalart and S.R. Allmaras in the early 1990s. It was designed for use mainly in solving aerodynamics problems [29]. While it still makes many assumptions, just like the $k - \epsilon$ model made, it is generally considered more robust in most instances than its $k - \epsilon$ counterpart [26]. The Spalart-Allmaras model is also only a single equation, whereas the previous model required two. Another one of its advantages is that it will produce better results on a coarser mesh than the $k - \epsilon$ model will. COMSOL uses a differential form of the equation, but omits the trip term used to induce boundary layer separation [26]. One key note for this turbulence model, as with most other models as well, is that it should not be used to determine the point at which the flow transitions from laminar to turbulent [29]. This is a very difficult problem to solve that is still not fully understood.

When using the Spalart-Allmaras turbulence model for the *High Mach Number Flow* physics, the user is able to select a no slip wall boundary condition. This is not available for the $k - \epsilon$ model discussed previously. Since the $k - \epsilon$ model only solves to the point at which the logarithmic and viscous sublayers meet, the full boundary layer is not resolved. For Spalart-Allmaras, the boundary layer is resolved and additional constraints are put in place for the velocity at the wall.

$$\boldsymbol{u} = 0$$

23

$$\tilde{v} = 0$$

The above constraints state that all three components of the velocity vector as well as the fluctuations must be zero at the wall [26]. For the full derivation of the Spalart-Allmaras turbulence model, see [26, 29].

3.3.2.3. Comparison of Models

In order to visually compare the effect of each of the turbulence models and wall boundary conditions, a plot is shown below in Figure 3.2. This figure shows the boundary layer profile for all three wall boundary conditions from the bottom wall to the centerline of a 0.5 *in* high duct. As expected, the slip wall shows a uniform velocity profile, whereas the *wall functions* and *no slip* boundaries show a typical velocity profile for flow over a flat plate or duct.
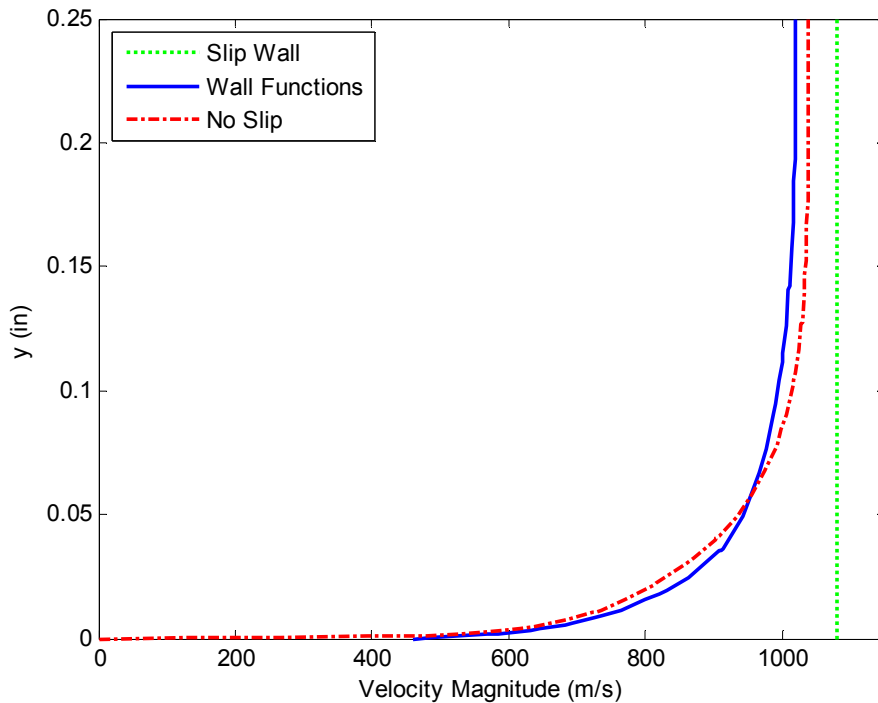
Figure 3.2: Velocity profile through boundary layer of Mach 2 flow over a flat plate with different wall boundary conditions. Slip wall and wall functions use $k - \epsilon$ turbulence model and no slip uses the Spalart-Allmaras model.

24

3.3.3. Solvers

COMSOL Multiphysics contains both direct and iterative solvers. For the CFD applications, COMSOL utilizes the built-in iterative solvers. This allows the software to use a sort of "guess and check" method and to approach the solution gradually. As the number of iterations increases, the error estimate decreases until the solution has an error on the order of 10^{-3} for the default setting, or a user-defined value [30]. The default number of iterations is 300 but this is not sufficient for every type of problem. The iterative solvers use a method known as the conjugate gradient method for linear systems [30]. This method was originally presented by *Hestenes* and *Stiefel* [31]. There are five key points that the method follows in order to reach a solution [31]:

- It is a simple, repetitive method that uses as little storage as possible

- Insures rapid convergence to reach a solution

- Round-off error must be stable

- Ideally, each step yields a better solution than the previous iteration

- The method uses as much of the original data as possible for each iteration

For more detailed information on the methods used by COMSOL, see [30,31].

3.3.4. Convergence Tricks

High Mach number flow problems are some of the most difficult simulations to get to converge that can be run using COMSOL Multiphysics [32]. It can take a lot of time and effort to set up the simulation and the solvers just right in order to find a solution. Thankfully, there are several tricks that can be used to aid in this process.

If it is necessary to solve for the properties in the boundary layer using the no slip wall condition, it is easier to first start by solving the same model using a slip or

25

wall functions boundary condition. Through experience, it has been found for the *High Mach Number Flow* physics that there is a much higher rate of convergence for simulations that utilized all three wall boundary conditions rather than just *wall functions* and a *no slip* wall condition. In order to use all three conditions, a series of three studies must be implemented. The example below is shown for a series of *stationary* studies and the *High Mach Number Flow* physics.

- Study 1: *Stationary* study that utilizes a *Slip* wall condition for the $k - \epsilon$ turbulence model.

- Study 2: *Stationary* study that is set up using the *Wall Functions* boundary condition for the $k - \epsilon$ model. The dependent variables being solved for are initialized using the previous solution from Study 1.

- Study 3: The turbulence model must first be changed to *Spalart-Allmaras* before changing the wall condition to *No Slip*. Study 3 is then added to the model builder tree, but in this case a *Stationary with Initialization* study is required. The $k - \epsilon$ model allowed a *Stationary* study to be added, but this particular turbulence model requires a different predefined study type. This particular type of study has two steps, both of which must be initialized using the solution from Study 2.

Another method that was implemented for aiding in convergence is to use an auxiliary sweep to decrease the viscosity, in turn ramping up the Reynolds number. This or a similar method is highly recommended by COMSOL for problems using the *High Mach Number Flow* physics [32-35]. The easiest method for implementing this sweep, is to first define a variable to use for the sweep under the global definitions. It

26

can then be multiplied by the viscosity in the fluid properties of the physics branch. An auxiliary sweep is set up for each of the three studies above under the *Study Extensions* section of the study node. After enabling the auxiliary sweep, the variable that was defined previously is selected and the values over which to sweep are placed in the *Parameter value list.* In general, a four part sweep (1000, 100, 10, 1) is sufficient for solving the problem. However, in some cases, only a two (10, 1) or three part (100, 10, 1) sweep is necessary. Each problem is different and must be set up only using these methods as general guidelines.

A third method that can be used in some cases is to define a set temperature on a boundary so that COMSOL does not try to calculate a negative temperature [32]. However, for simulations where the heat release is undesirable, this is not possible. In most cases this can be avoided, it is just shown for completeness.

Chapter 4: Isolator

The purpose of the isolator in the dual-mode scramjet setup is to allow for a static pressure rise through the generation of a shock train. The pressure must rise to match that due to combustion downstream. As the name implies, the isolator also serves the purpose of separating the combustion region from the inlet to help prevent the pressure rise from propagating upstream and causing inlet unstart. This is when the shock train is disgorged by the inlet and the flow becomes subsonic throughout the scramjet. This is highly undesirable and causes immense performance losses. In a true scramjet engine, the isolator is either unnecessary or can be greatly reduced in length. For the model scramjet that was the work of this research, the isolator was needed due to isolate the shock train caused from thermal choking.

4.1. Geometry and Model Set-up

The isolator portion of the dual-mode scramjet being modeled is a simple rectangular duct. In the experimental setup, it had a 0.5 *in* square cross section and was 8.5 *in* long [1]. Upstream of the isolator duct was a vitiated heater and nozzle block that allowed for the simulation of a high enthalpy flow. This allowed for a higher simulated Mach number than the laboratory equipment could produce. However, due to these limitations in testing equipment, the flow through the scramjet was limited to about Mach 2. In the simulations that are presented in this chapter, only the isolator was modeled – not the vitiated heater or nozzle block. Therefore, only an 8 *in* long section was modeled.

28

4.1.1. Physics

After the geometry was completed, the *High Mach Number Flow* physics had to be added to the model. For the first study, the $k - \epsilon$ turbulence model was used with the *slip* wall boundary condition. The estimated initial values and inlet conditions are shown in Table 4.1.

Table 4.1: Estimated Isolator Inlet Conditions. Based on the values from the experiments [1].

Parameter	Symbol	Value	Units
Mach Number	M_1	2.04	-
Static Temperature	T_1	700	K
Static Pressure	P_1	83.3	kPa
Total Pressure	P_{o_1}	684	kPa
Duct Height Reynolds Number	Re_h	154,000	-
Total Fuel Mass Flow Rate	$\dot{m}_{tot}$	0.377	g/s

As discussed in section 3.3.3, two of the most reliable methods to aid with convergence for *High Mach Number Flow* problems are to a) first solve the problem without a boundary layer and use it to initialize the flow field with a boundary layer and b) to artificially ramp up the Reynolds number by decreasing the viscosity. Both of these methods were utilized when solving this problem.

The outlet boundary condition was set to *Hybrid*. This condition supports both subsonic and supersonic conditions [26] as would be found in a flow with a subsonic boundary layer and supersonic core. This boundary condition requires the pressure to be defined at the outlet. For the isolator simulations, the pressure was set to the measured experimental values at the x/H = 0 location for the equivalence ratio being

29

modeled. This corresponds to the pressure at the outlet of the isolator. For these simulations, no additional mass or heat sources were added.

4.1.2. Mesh Convergence Study

The mesh was set to *Physics-Controlled Mesh.* This allows COMSOL to automatically generate the boundary layer mesh, as well as choose the fineness of the mesh throughout the model. In order to ensure that the mesh being used resulted in a converged solution, a series of tests were done using various mesh sizes. By default, COMSOL generates a "normal" mesh size when using *Physics-Controlled Mesh*. This can be changed manually to one of nine predefined element sizes ranging from extremely coarse to extremely fine. Ideally, the final mesh will be fine enough to result in an accurate solution, yet not too fine as to increase computational cost so much so as to negate the effects of the incremental increased accuracy. The simulation run times and degrees of freedom required for each mesh element size that was tested can be found in Table A.2 in the appendices.

Table 4.2: Comparison of Simulations as a Function of Mesh Element Size.

Element Size	Number of Domain Elements	Number of Boundary Elements	Total Solution Time for all Studies
Coarse	41426	1226	2583 s (43:03)
Normal	95288	2576	10059 s (02:47:39)
Fine	214616	4938	17469 s (04:51:09)

As shown in Table 4.2, there is a drastic increase in computational cost and simulation time as the mesh element size is decreased. If very fine accuracy is required, then the cost is unavoidable. However, the minimal increase in accuracy is usually not worth the extra time required in most cases. After running the three cases as seen in Table 4.2, the results were compared to determine the best mesh to use for this particular

30

setup. It was chosen to use the Normal mesh due to its great agreement with the *Fine* mesh, but taking only half as much time to converge to a solution.

4.2. Results

4.2.1. Comparison with Experimental Data

The model scramjet was run for a variety of combustor equivalence ratio values between 0 and 0.20 [1]. In order to test COMSOL's ability at generating some of the flow structures that were seen in the experiments and that are typical to these types of airbreathing engines, each of the Φ cases were simulated. The shock structures for each of these cases are shown in Figure 4.1.

It can be clearly seen in Figure 4.1 that as the back pressure ratio is increased

(a) $\Phi = 0.00$
(b) $\Phi = 0.04$
(c) $\Phi = 0.08$
(d) $\Phi = 0.12$
(e) $\Phi = 0.16$
(f) $\Phi = 0.20$
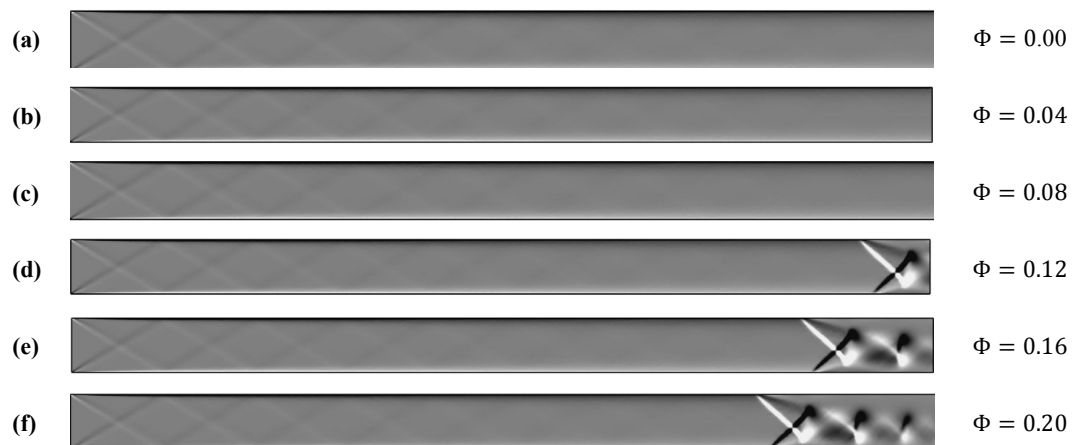
Figure 4.1. Simulated vertical density gradient for all fuel flow conditions.

past a certain critical value, a shock train forms and begins to propagate upstream to accommodate the higher back pressure. By plotting the pressure along the top surface

31

of the isolator (Figure 4.2 (a)), the simulations can be compared to the experimental

results (Figure 4.3 (b)).
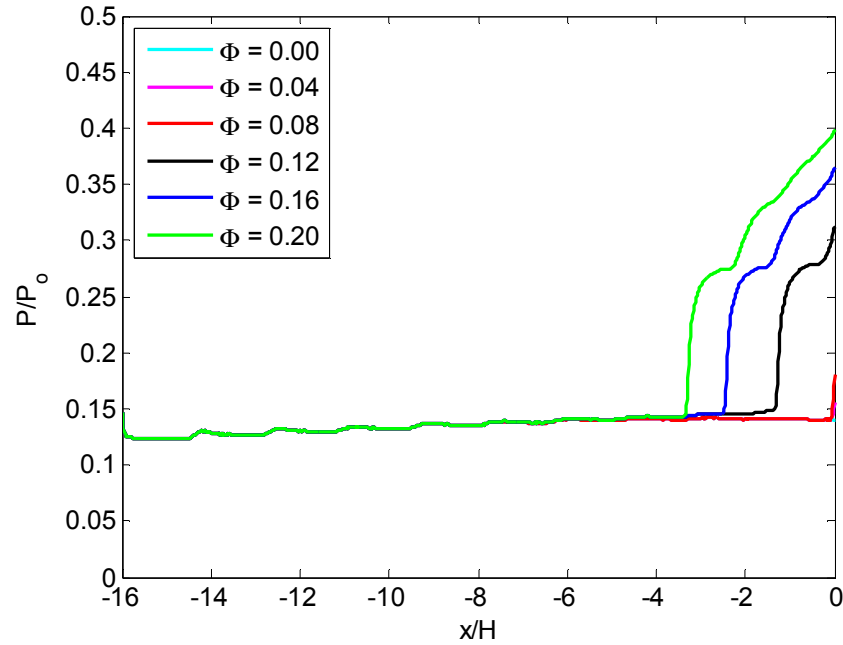
a) Simulated static pressure
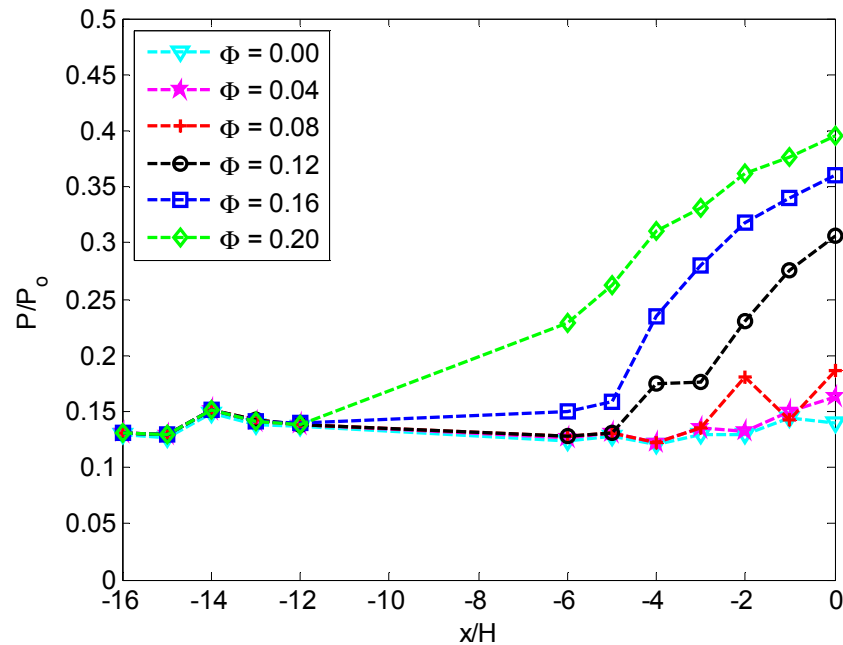
b) Experimental static pressure. Data from [1].

Figure 4.2: Simulated (a) and experimental (b) static pressure measurements along the top wall of the isolator for all Φ cases.

32

When comparing Figures 4.1 and 4.2 (a), it is evident that a longer shock train produces a higher pressure ratio. Each pressure at the outlet of the isolator was able to be matched with the experimental data as shown in Figure 4.2 (b). However, the shock train starting location varies widely between the simulations and experiments. This is due to the nature of the shock train that was generated by COMSOL. A closer look and comparison can be seen in Figures 4.3 and 4.4. There are two main types of shock trains – those with an oblique and those with a normal shock structure. The normal shock structure that was generated by COMSOL, shown in Figure 4.3 (b) looks almost identical to that seen in isolator experiments in Figure 4.3 (a) by *Geerts* [36]. However, the model scramjet by *Aguilera* [1] showed an oblique shock structure as seen in Figure 4.4 (b).
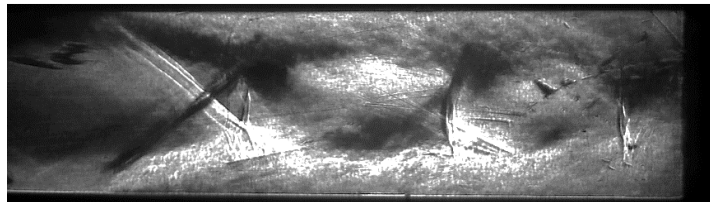
(a) Experimental schlieren photograph visualizing vertical density gradient in an aspect ratio 3 isolator [36].
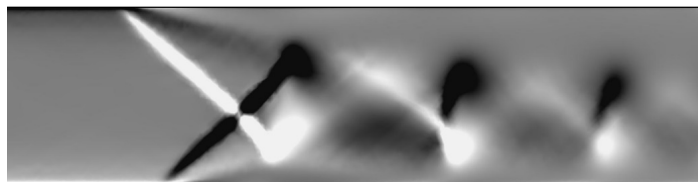
(b) COMSOL simulation showing vertical density gradient in isolator of dual-mode scramjet engine for $\Phi = 0.20$. Portion of Figure 4.1(f) shown.

Figure 4.3: Experimental and simulated shock trains in a constant area duct. Black and white indicate a negative and positive density gradient, respectively.

(a) COMSOL simulation for baseline reacting case with $\Phi = 0.12$ showing vertical density gradient in isolator. Far upstream and has been cut off in this illustration. See Figure 4.1 (d) for full isolator simulation.
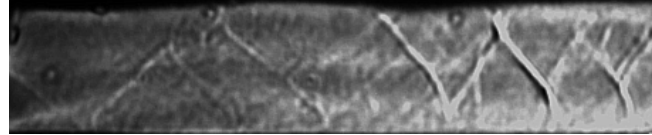
(b) Experimental schlieren image for baseline reacting case with $\Phi = 0.12$ [1].

Figure 4.4: Shock train structure as seen in simulated (*a*) and experimental (*b*) schlieren images for isolator from $x/H = -4$ to $x/H = 0$.

A possible explanation for this difference in shock structures is the boundary layer thickness. According to *Smart* [9], thicker boundary layers typically produce longer shock trains. Without having boundary layer thickness measurements from the model scramjet, it is difficult to compare with the thickness from the simulations. More experimental data might have led to a more accurate CFD model.

4.2.2. Discrepancies

As mentioned in the previous section, one of the largest discrepancies between the simulated results and the experimental data is that COMSOL generated more of a normal shock train structure, whereas an oblique shock structure was seen in the experiments. This oblique structure allowed for a more gradual pressure rise throughout a longer section of the isolator. It also reduced the stagnation pressure loss when

compared to a normal shock structure because more stagnation pressure is retained across an oblique shock. This is beneficial for engine performance characteristics. Conversely, the normal shock structure produced by COMSOL has a much steeper rise in pressure over a much shorter axial distance.

Shock trains are an inherently three-dimensional structure. In a square duct such as the model scramjet isolator, there is a boundary layer on all four interior walls. Due to surface roughness, static pressure points, or other irregularities, the boundary layer might be different on each wall. This can cause an asymmetric shock train structure. All of the simulations that were presented were modeled in two-dimensional space to reduce the computation time from being on the order of days to hours. A three-dimensional simulation was run using a shorter duct but with the same mesh and wall boundary conditions. The *wall functions* boundary took more than twenty-four hours to run. Due to the extremely high cost, the *no slip* wall condition was not run and it was chosen to stick with the 2-D model.

Chapter 5: Combustor

5.1. Approach

After some initial testing, it was found that the best approach was to model the isolator and combustor separately rather than as a single model. The benefits were four-fold: it allowed for more control and fine tuning of each component separately, greatly reduced the total simulation run time, allowed for generation of the shock train pattern in the downstream portion of the isolator, and greatly aided with convergence. In addition, simulating the parts separately gave the approximate isolator exit conditions to allow for the focus to be more on the heat release pattern and the individual effect of the area divergence, cavity, and fuel injection on the pressure profile along the top wall. Rather than spending much more time only running simulations, by splitting the geometry into the two distinct parts, the focus could shift to the heat release and subsequent performance characteristics for each case.

5.2. Model Set-Up

The geometry for the combustor will follow in section 5.3 below. The same general process that was presented in section 4.1 was used for the combustor simulations that are presented in this chapter. After setting up the geometry as a Bézier polygon comprised of a series of line segments, the *High Mach Number Flow* physics were added. Just as for the isolator, the first study was set up using the *Slip* wall boundary condition for a *Stationary* study. After the solution had finished, a second

36

study was added utilizing the *Wall Functions* boundary condition and was initialized using the solution from Study 1. This was followed by a third *Stationary with Initialization* study for the *No Slip* condition as part of the *Spalart-Allmaras* turbulence model. Both steps of this study were initialized using the solution from Study 2. The auxiliary sweep was performed for these simulations and more information can be found in Appendix A1.

In the case of all of the combustor simulations, the outlet boundary was set to *Hybrid* at 1 *atm*. In some cases, the flow was expected to be thermally choked. In others, it was expected to remain supersonic. The *Hybrid* boundary condition allows either of these cases to exist. The outlet pressure was chosen to most accurately reflect the conditions seen in the experiments where the combustor exhausted into roughly STP conditions. The inlet conditions for each simulation will be discussed in more detail in sections 5.3 and 5.4.

5.3. Simulation of Experimental Conditions

For the model scramjet, *Aguilera* ran two different configurations: the baseline model and a fin-guided geometry that placed a triangular fin just upstream of the fuel injection orifice [1]. This fin allowed for better fuel penetration into the cross-flow. For detailed information, diagrams, and analysis, see section 4.2 of [1]. It was chosen to leave out this more detailed information as the main focus of this research was on the effect of heat release location and performance characteristics for different modes of operation. The basic ideas and concepts will try to be explained when deemed necessary for understanding.

5.3.1. Model Scramjet Combustor

5.3.1.1. Geometry and Physics

The combustor geometry used in the experiments [1] is more complex than that of the isolator. Throughout the combustor section, there is a constant 2 *degree* linear divergence. Area divergence is a common feature to many scramjet combustors [1,6,15] as it is a relatively simple method for reducing the chance of thermal choking. Also included in the combustor geometry is a cavity for the purpose of flame holding. A mechanism such as a cavity or a v-gutter is typically necessary to allow for the flame to stay lit in a supersonic cross-flow by creating a small region of low-speed recirculating flow [1,20]. The geometry for the combustor is shown in Figure 5.1.
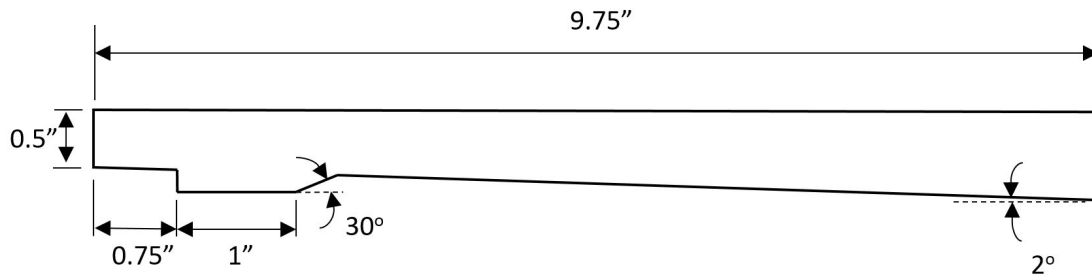
Figure 5.1: Combustor geometry with cavity. The leading edge of the cavity is recessed about 0.2 *in* into the bottom wall. Fuel injection location is at the leading edge of the bottom wall. *Figure adapted by author from* [1].

This geometry was created based off of the model scramjet setup designed by *Aguilera* [1]. In the experimental setup, the 3-D geometry had a depth of 0.5 *in*. However, it was modeled in COMSOL in two-dimensional space in order to reduce computational cost and aid with convergence. This 2-D model can be used to parametrically vary certain parameters and see how they affect the pressure distribution much easier than in a full 3-D model. Once the 2-D model is set up and refined, a 3-D model could be simulated in the future.

38

In some cases, the simulation was run with fuel injection. Appendix A2 shows the derivation for calculating the fuel injection slot width. In the model scramjet, the fuel was injected through a circular orifice located at the centerline along the bottom wall of the scramjet at the entrance to the combustor [1]. This can be seen in Figure A2.1. This circular orifice in the 3-D scramjet had to be transformed into a 2-D slot of unit depth in the spanwise direction. The fuel mass flow rate was then calculated to ensure that the same mass flux was occurring in the 2-D model as seen in the experiments. For the cases is which this was modeled, a secondary inlet, of length w_f, was added to the bottom wall at the leading edge of the combustor geometry.

Due to the lack of a chemically reacting module, the combustion zone in the scramjet was modeled using a heat source in COMSOL. The software allows heat sources to be modeled in three different fashions: as a point, line, or domain. The heat release was modeled using a *Domain Heat Source* because it most accurately represents what was seen in the experiments [1]. The chemical reaction took place over a certain volumetric domain of the combustor, not at a single point or along a 2-D line. Similar to the fuel injection, the derivation for the maximum total amount of possible heat release, Q_{max}, is found in Appendix A2. The total amount of heat release varies between the baseline and fin-guided model scramjet setup due to slightly different combustor equivalence ratios. The location and size of the heat release domain also vary depending on the case being simulated.

The location of the heat release domain was estimated using chemiluminescence data gathered during the experiments [1]. Optical access to the model scramjet was limited so this data is only available for a small region of the

39

geometry. In cases where the flame extended beyond the visible region, the data was extrapolated in order to estimate the approximate heat release location. This was not an issue for this particular case being simulated, however. For the experimental baseline case with $\Phi = 0.11$, the heat release took place mostly in the region of the cavity. This was evident in the OH* chemiluminescence data [1]. Because the majority of the combustion was in the cavity, this is where the heat release domain was placed for the cavity simulation. This is shown in Figure 5.2, along with the corresponding chemiluminescence data.
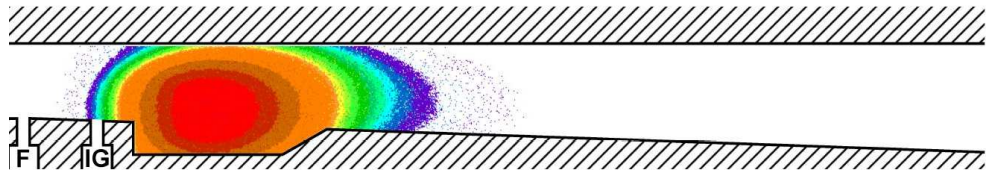
(a) OH* chemiluminescence data for baseline case with $\Phi = 0.11$ [1]. The majority of the heat release is seen over the cavity region of the combustor.
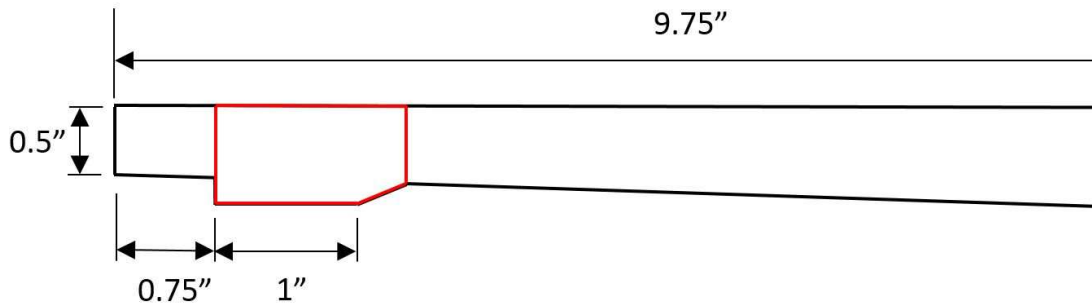
(b) Portion of simulated combustor showing the heat release domain (red) that was used. Downstream of $x/H = 14$ is not shown in this illustration in order to match the viewing window in (a). See Figure 5.1 for full geometry.

Figure 5.2: Experimental chemiluminescence data (*a*) and simulation setup (*b*) for cavity combustor simulation at $\Phi = 0.12$.

Please note that in the experiments, data was gathered over many different individual runs. While the combustor equivalence ratio for the cases being modeled were all between 0.11-0.12, all of the simulations were run assuming $\Phi = 0.117$ based

www.manaraa.com

on the test conditions available in Table 5.5 of [1]. However, the experimental data presented herein will be referred to by the equivalence ratio in which the original author presented it. This explains the discrepancy between equivalence ratios shown in Figure 5.2.

5.3.1.2. Thermally Choked Model Scramjet Results

Because the isolator and combustor were modeled separately, it added another unknown into the simulations. Due to flow features such as a shock train and boundary layers, all of the parameters such as the Mach number, temperature, and pressure have some profile at the exit plane of the isolator. Because of the way that COMSOL is set up, there is no trivial manner in which to export the profile as a function of the y-
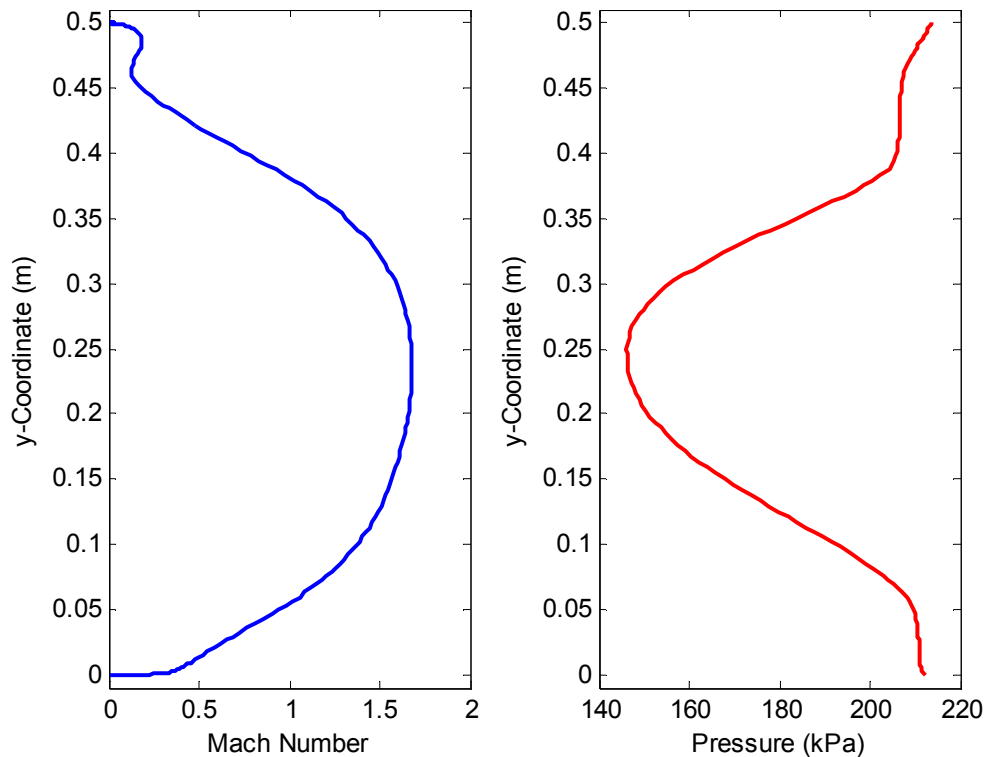
Figure 5.3: Simulated Mach number (*left*) and pressure (*right*) profiles at isolator exit boundary for baseline $\Phi = 0.12$ simulation.

41

coordinate from the isolator and apply it to the inlet boundary of the combustor. While the full profiles would provide the most accurate results, an average value had to be used. Sample isolator exit profiles were shown in Figure 5.3.

In order to find the best inlet conditions to use for the cavity combustor model presented here, a series of tests were run with varying the inlet conditions within the ranges that were seen in Figure 5.3. COMSOL defines the HMNF inlet with a constant value, unlike the profile that is to be expected for flow with a no slip wall. Therefore, the inlet conditions were estimated from the isolator simulation and adjusted based on the experimental pressure data. The data is not expected to match perfectly because of
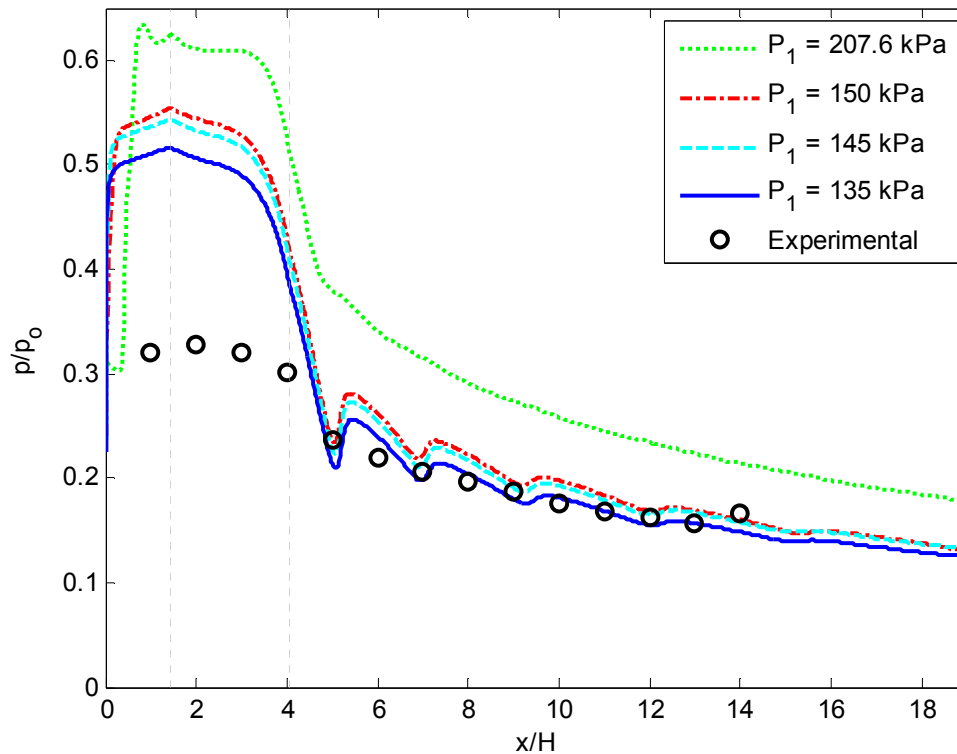
Figure 5.4: Pressure along the top wall as a function of inlet static pressure. Same heat release domain size, location, and intensity for all cases. Vertical dashed lines represent beginning and end of heat release as seen in Figure 5.3 (b). Experimental data from [1].

42

the many simplifications that have been made for these models. However, it is hoped to at least match the general trends.

As expected, it was shown in Figure 5.4 that the results are greatly affected by the inlet conditions. However, for the remainder of these cavity simulations, the inlet pressure that was chosen was 135 *kPa* because it matched the experimental data most closely.

5.3.2. Simplified Scramjet Combustor

5.3.2.1. Geometry and Physics

In addition to the geometry shown in Figure 5.1, a more simplified geometry was also used. This simplified combustor consisted of a duct of the same basic dimensions, but did not contain the fuel injection or cavity that was present in the previous combustor geometry. The simplified combustor is shown in Figure 5.5. As will be discussed in more detail later, this simplified combustor geometry allowed for learning the effect that each part of the combustor has on the pressure data along the top wall. The effects of fuel addition, the cavity, area divergence, and heat release location were all analyzed using wither the simplified or cavity combustor geometry in an attempt to better understand the flow field within.
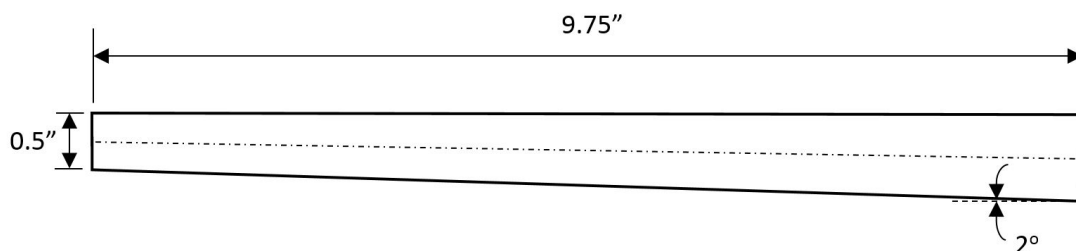
Figure 5.5: Simplified combustor geometry based off of original combustor. Also denoted is the centerline between the top and bottom surfaces.

43

The inlet conditions for this simplified model were based on the pressure measurements from the fin-guided combustor at the $x/H = 0$ location, or the start of the combustor. Using the measured pressure data and assuming that the stagnation temperature remains relatively constant throughout the isolator, the inlet pressure, temperature, and Mach number are calculated for this particular problem. These values were required to initialize the model before solving. Just as with the combustor geometry with the cavity that was presented earlier in section 5.3.1, the outlet was prescribed to be *Hybrid* at 1 *atm*.

To determine the approximate location of the heat release zone for the supersonic combustion case, the chemiluminescence data again proved extremely valuable. This is shown in Figure 5.6. In this particular instance, the heat release occurs over a much larger region due to the increased fuel penetration caused from the fin [1]. The localized intensity is much lower than for the thermally choked case presented before because roughly the same amount of heat is distributed over an area that is several times as large. The fin itself was not modeled but an illustration can be seen in Figure A2.1.

Before any comparisons could be made between the cavity and simplified combustors, the simplified geometry was run using a range of heat release values. This was done to determine the estimated amount of heat release that was present in the experiments. A non-reacting simulation was run as well in order to see the effect that heat release has compared to the area expansion that is present in the combustor. Rayleigh flow and expansion both affect the flow speed and thermodynamic properties.

44

The effects of each can be calculated individually to show how much of an impact they

will have on the flow. Presented in *Shapiro*, the influence coefficients for quasi-one-
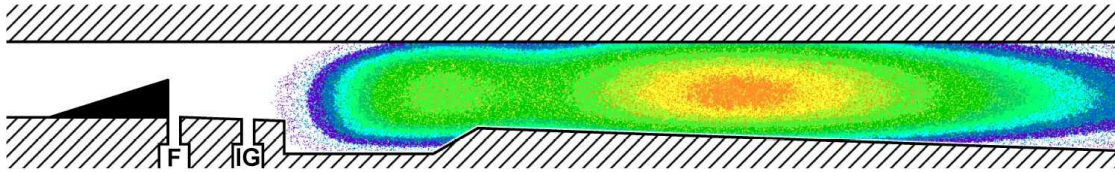
(a) OH^* chemiluminescence data for fin-guided case with $\Phi = 0.12$ [1]. The majority of the heat release is seen downstream of the cavity region in the diverging area portion of the combustor.
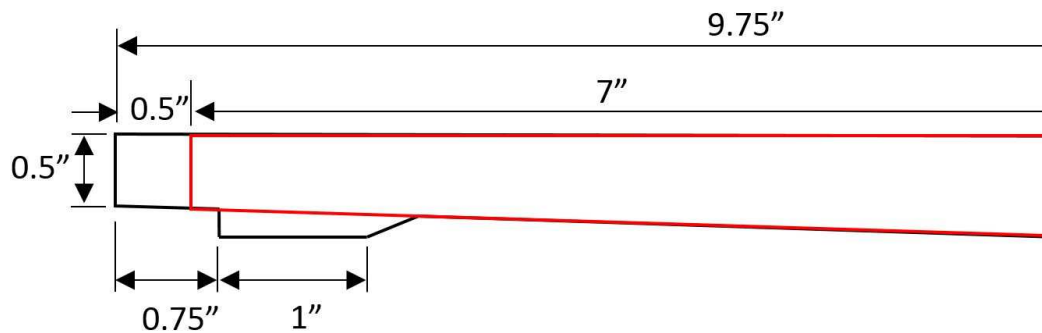
(b) Portion of cavity combustor showing the heat release domain (red) that was used. Downstream of $x/H = 14$ location is cut off in this illustration in order to match the viewing window in (*a*).
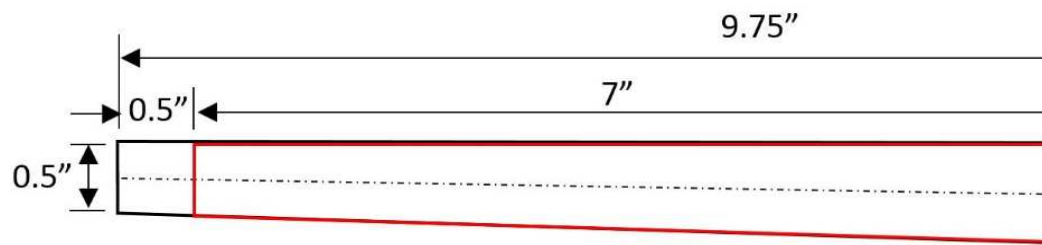
(c) Portion of simplified combustor showing the heat release domain (red) that was used. Downstream of $x/H = 14$ location is cut off in this illustration in order to match the viewing window in (*a*).

Figure 5.6: Experimental chemiluminescence data (*a*) and simulation setup (*b,c*) for supersonic combustion simulation at $\Phi = 0.11$. In both (*b*) and (*c*), the heat release domain is a simple 7 *in* long trapezoid extending from the top to bottom wall, not including the cavity.

dimensional flow allows for the derivation of a partial differential equation that takes into account the effect of area expansion, heat release, mass injection, and more on flow properties such as Mach number, temperature, or pressure. [37]. For more information, see Appendix 3. It was anticipated that the effects of heat release would overpower those of the area divergence at some critical value. This has been shown in Figure 5.7. Once the total heat release nears about two-thirds of the maximum LHV of the fuel available for this particular combustor equivalence ratio, the heat release and area divergence essentially negate the effects of one another and the pressure remains relatively constant. Above this critical value, heat release dominates, and below, the
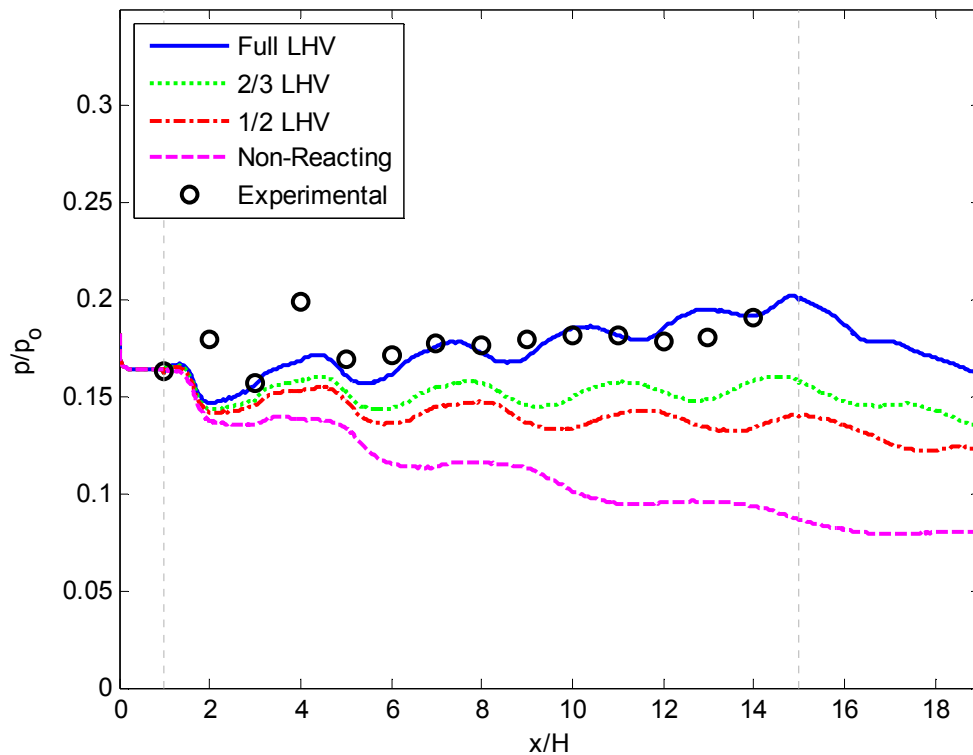
Figure 5.7: Static pressure along the top wall for the simplified combustor simulations as a function of the heat release intensity. Inlet conditions and heat release location, except for the non-reacting case, remain the same for all. Experimental data from [1].

area divergence has more of an effect. Each equivalence ratio will have a different critical value. For cases in which there is less fuel available, the heat release may not be able to overcome the expansion. Conversely, at higher equivalence ratios, there is more fuel available to burn, leading to a higher total heat release assuming that there is enough oxidizer and time for the reaction to take place. This would lower the critical value necessary to overcome area divergence.

5.3.2.2. Simplified Combustor Results

After the total amount of heat release was determined, as shown in Figure 5.7, the simplified combustor geometry could be compared to that with the cavity. The same cavity combustor geometry that was used for the case before was used again for the supersonic combustion case. The inlet conditions and heat release location and magnitude were updated to reflect the conditions that were seen in the fin-guided experiments [1]. As mentioned previously, the simplified combustor geometry was also modeled with these same inlet conditions and heat release properties for comparison.

The geometry for each case, the heat release domain location, and the chemiluminescence data gathered in the experiments was presented in Figure 5.6. During the experiments, optical access was fairly limited, so there is no intensity data available downstream of the zone shown in the figure. Therefore, the approximate location for the end of the heat release had to be extrapolated based on the available data. One of the parametric sweeps that will be presented in a later section shows the effect of increasing the length of the heat release domain.

Based on the results shown in Figure 5.7, the maximum possible amount of heat release most closely matches the experimental data. Therefore, that is the value that

47

was used to compare against the combustor geometry containing the cavity. The same simple trapezoidal domain with the same amount of heat release was used for both geometry setups, as shown in Figure 5.6. Because most of the combustion took place downstream of the cavity for the fin-guided case, as seen in Figure 5.6 (a), the cavity was not included in the heat release domain itself. This also allowed for a more equal comparison between the cavity and simplified combustor models.
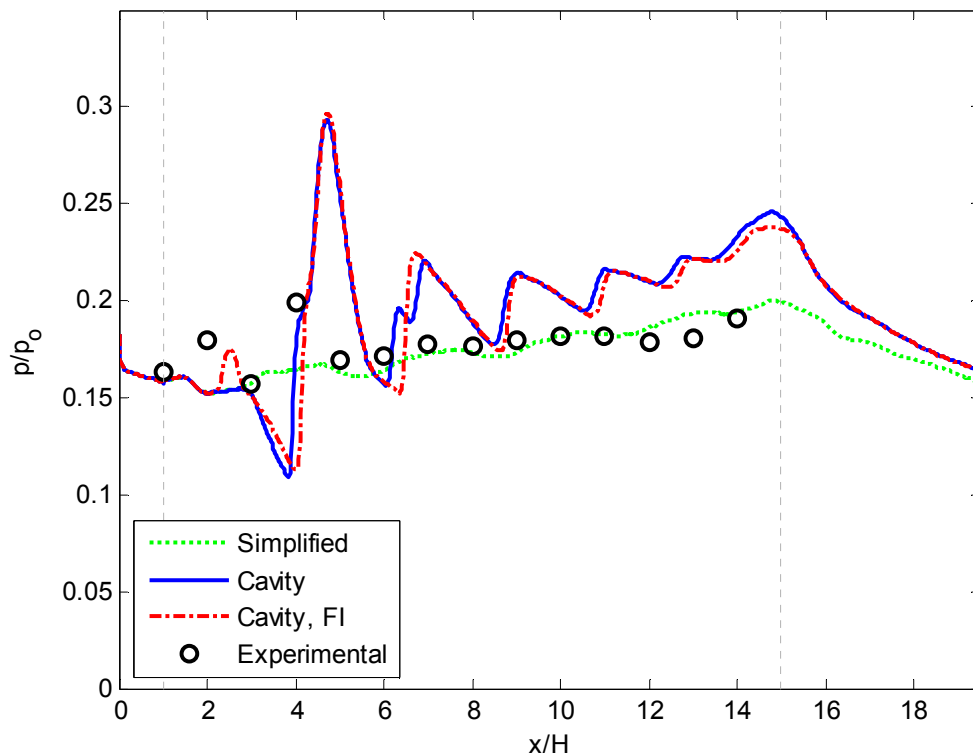
Figure 5.8: Comparison of simplified combustor with cavity, and cavity with fuel injection. Note: fuel injection was placed at $x/H = 1$ where the igniter was located in the experiments. Experimental data from [1].

It can be seen that the simplified combustor most closely matched the experimental data. However, it must be reiterated that model is the furthest from the actual model scramjet setup of all of the cases that have been simulated. On the contrary, the two results that are shown for the cavity combustor use the same cross-

48

sectional geometry as the model scramjet, only that it was modeled in two dimensional space. Fuel injection was included in one of the simulations shown in Figure 5.8 as evidenced by the small peak just downstream of $x/H = 2$. This peak represents the location where the injection induced shock impinges on the upper wall of the geometry. This can also be seen in the velocity surface plot shown in Figure 5.9.
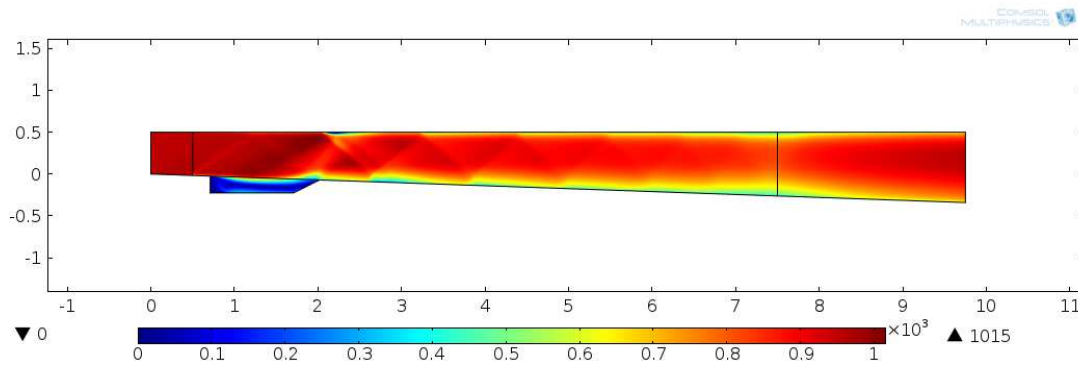
Figure 5.9: Velocity surface plot from cavity combustor geometry with heat release and fuel injection. Fuel injection-induced shock can be seen just upstream of the cavity. Axes are in *inches* and color legend is the velocity scale. Units are in *m/s*.

However, the fuel injection is of small enough magnitude that it has little effect on the flow downstream of the cavity. The ramp at the end of the cavity has much more of an effect on the overall flow field. The heat release domain was the same trapezoid as shown in Figure 5.6 (b). Also worth mentioning from Figure 5.9 is the velocity is zero or very close to it throughout the cavity. This supports the claim that the cavity is there to generate a region of low speed flow in order to support flame holding.

5.4. Effect of Flame Unsteadiness or Fluctuations

Now that it has been shown how the results can change depending on the geometry and inlet conditions that are used, the next step is to see what happens if the flame were to fluctuate in the streamwise or wall-normal directions (axial and vertical,

49

respectively). Since the simulations were computed in 2-D, there is no spanwise direction in which to vary the heat release pattern. This would be more directly related to the experimental results due to the very transient nature of the combustion process [1]. Since the simulations were modeled using a *Stationary* study, this transient behavior is not captured by these results. Parametrically changing the location of the heat release helps ensure that the results more accurately reflect what was seen and gives a better understanding of the influence of heat release location on the wall pressure. The experimental results that all of these simulations are compared to are a time-averaged pressure profile over a finite time span whereas the simulations are set up to reach a steady-state solution at one instant in time.

5.4.1. Thermally Choked Case w/ Cavity Fluctuations

The combustion process is highly transient as the flame fluctuates in intensity, size, and location. In order to test the effect of the flame shifting up or down in the cavity, the previous full cavity heat release domain, presented in section 5.3.1, was broken down into two equal parts. This allowed for the same heat release density to be used for each case.

Figure 5.10: Thermally choked cavity combustor with heat release domain broken into 2 equal parts by the centerline. Each part will be modeled separately with equal heat release densities and compared.

In Figure 5.10, the black dashed line in the cavity region denotes the centerline between the top and bottom walls. This was used as the dividing line for the "upper" and "lower" cavity for the simulations shown in Figure 5.11. The model was adjusted to change the heat release domain as shown above then the simulations were run using the same total amount of heat release as that in Figure 5.4. Due to the manner in which COMSOL defines heat release over a volumetric domain, half of the total area corresponds to twice the heat release density. In addition, the heat release was applied as a constant value per unit area. In reality, the combustion process could be much more localized or it could fluctuate very rapidly. Just as mentioned before, the purpose of
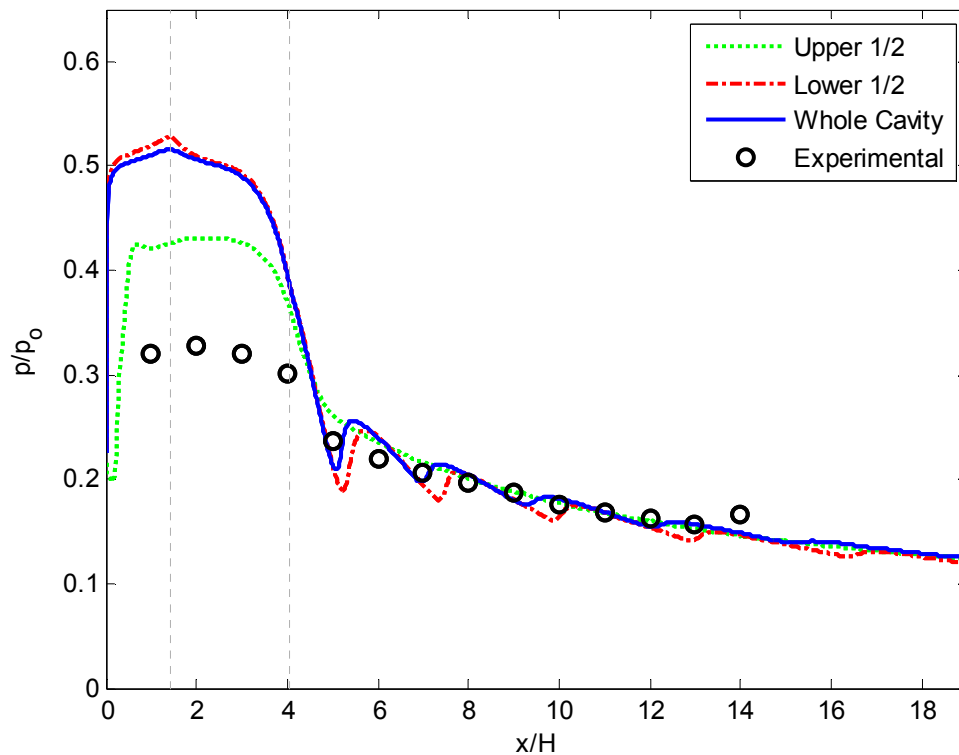
Figure 5.11: Pressure along the top wall as a function of heat release domain location. The heat release density is the same for all 3 cases but the domain is shifted in the y-direction. The upper and lower half denote from the centerline to the top or bottom wall, respectively. Experimental data from [1].

51

running these simulations is to test the feasibility of using a commercial software package to simulate an experimental scramjet setup. Getting the data to match exactly would require a much more complex simulation with a full 3-D solver, transient study, and chemically reacting flow model and could require a large number of iterations to optimize the solution. Shifting the heat release had a moderate impact on the static pressure along the top wall of the combustor, particularly over the location of the cavity. This implies that with a more complex model and enough iterations using various locations and heat release intensities, the experimental data could be reproduced more accurately.
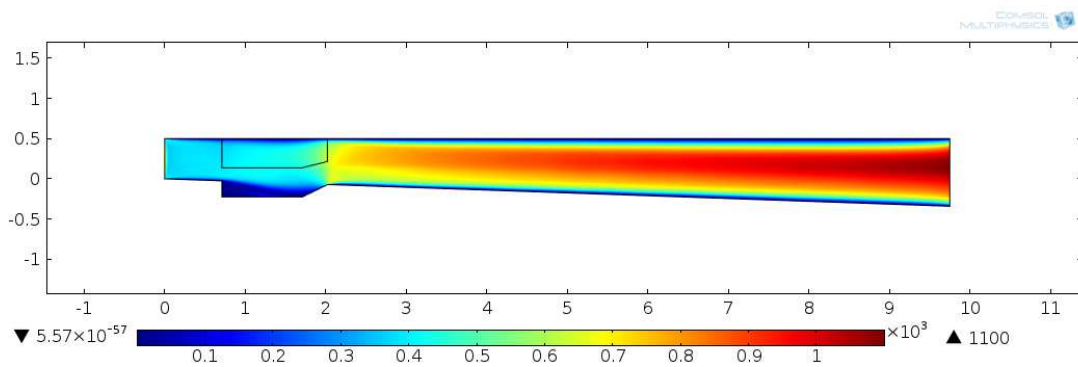
Figure 5.12: Velocity surface plot from cavity combustor geometry with "upper" cavity heat release domain. Units are in *m/s*.

In Figure 5.12 above, it is seen that the flow was thermally choked at the inlet. This is what causes the shock train to form in the isolator as shown in Figure 4.1. Both the "upper" and "lower" cavity simulations were thermally choked. However, after heat addition and the expansion caused by the end of the cavity, the flow reaccelerates downstream. Just as in Figure 5.9, the flow is near zero velocity in the cavity.

5.4.2. Simplified Supersonic Combustion Case w/Streamwise Fluctuations

The first fluctuation type that will be analyzed for the simplified combustor is in the streamwise direction. As was seen in the chemiluminescence data, the flame length can vary greatly from the lowest to the highest values of the combustor equivalence ratio.
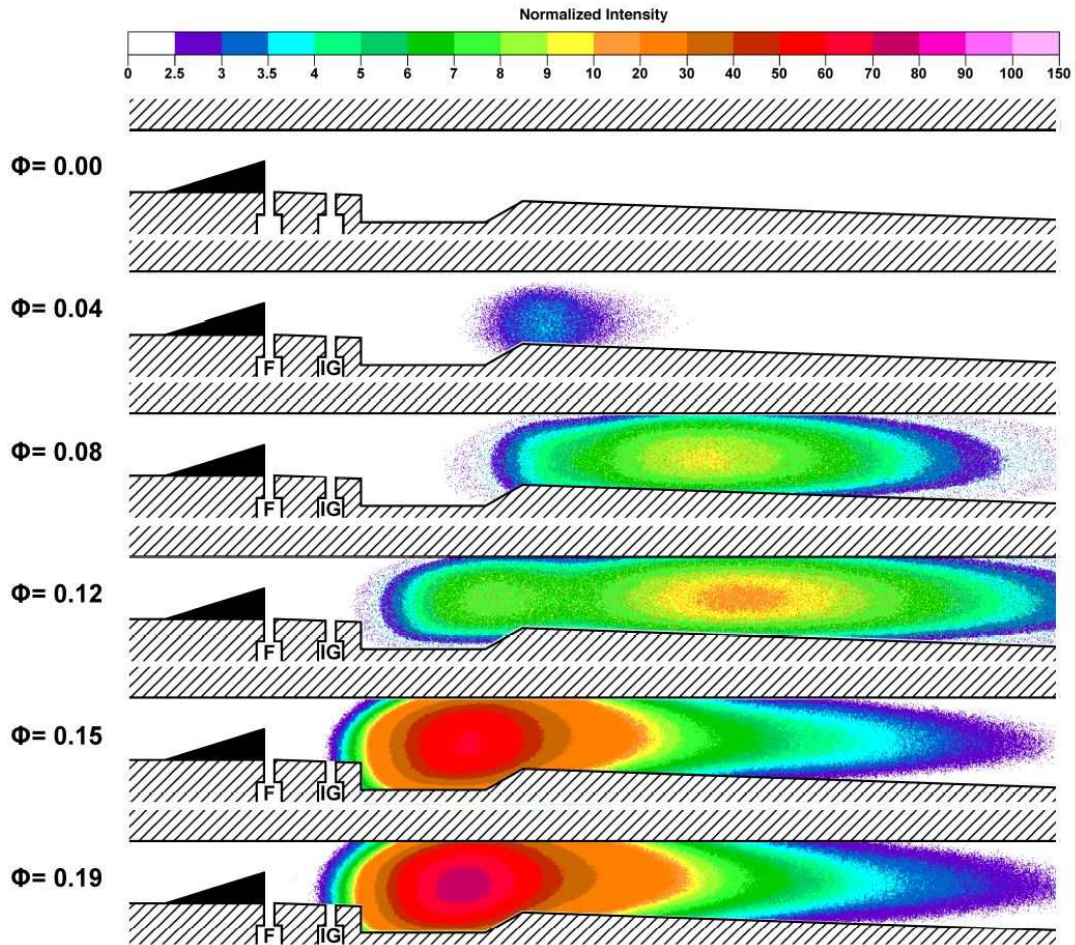
Figure 5.13: Chemiluminescence contours for fin-guided case as a function of combustor equivalence ratio. *Reprinted from* [1] *with permission from the author.*

The chemiluminescence contours by *Aguilera* [1], reproduced with permission in Figure 5.13, indicates the general region in which to expect the combustion to take place, but the flame will not be located in a single location – it will shift around in all directions, fluctuate in intensity, and have overall transient behavior. This causes the local minima and maxima of the pressure data to average out into a much smoother curve as seen in the experimental pressure data in [1].

Depending on the instantaneous flame length and subsequent heat release, the combustion zone can vary in the streamwise direction. This was replicated as a series of simulations with a different heat release domain length for each. This is illustrated in Figure 5.14.
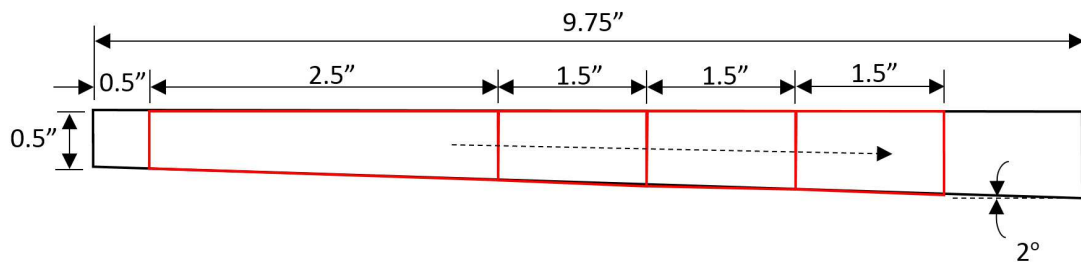
Figure 5.14: Simplified combustor with streamwise fluctuation in heat release domain. Starting location and total amount of heat release remains constant as the ending location moves further downstream.

In Figure 5.14, the heat release domain begins at the igniter location at $x/H = 1$ and ends at $x/H = 6$. It is then extended to $x/H = 9$, 12, and finally 15 in each subsequent simulation. The last case was shown previously as the simplified case in Figure 5.6 (c). The results from the above heat release domains are shown in Figure 5.15. In all cases, the inlet conditions, starting location, and total amount of heat release all remain constant. The heat release density varies as a function of the area of each domain – as the area increases by extending the domain further downstream, the heat release density decreases. Intuitively, as the heat release density decreases, so does the

54

risk of thermal choking. If the same amount of heat is applied over a larger area, it is

less likely to cause the flow to thermally choke and become subsonic somewhere in the
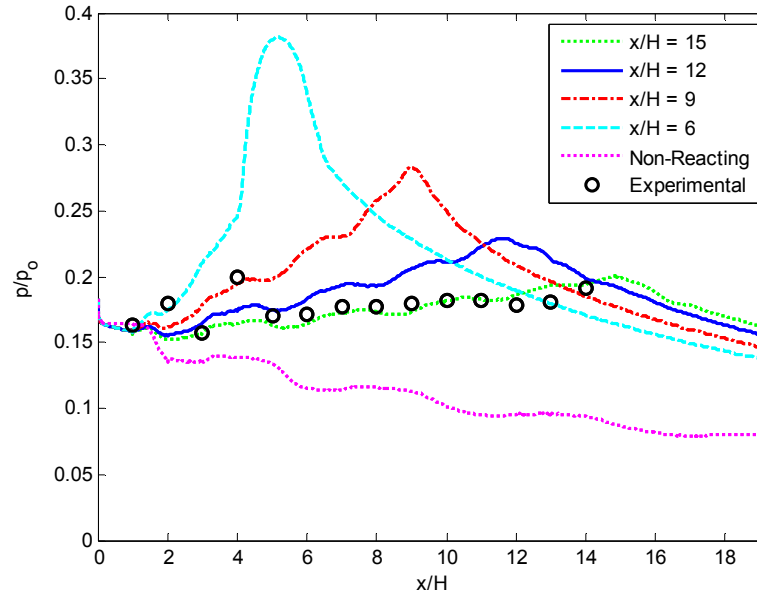
(a) Simulated static pressure along the top wall for simplified combustor. Experimental data from [1].
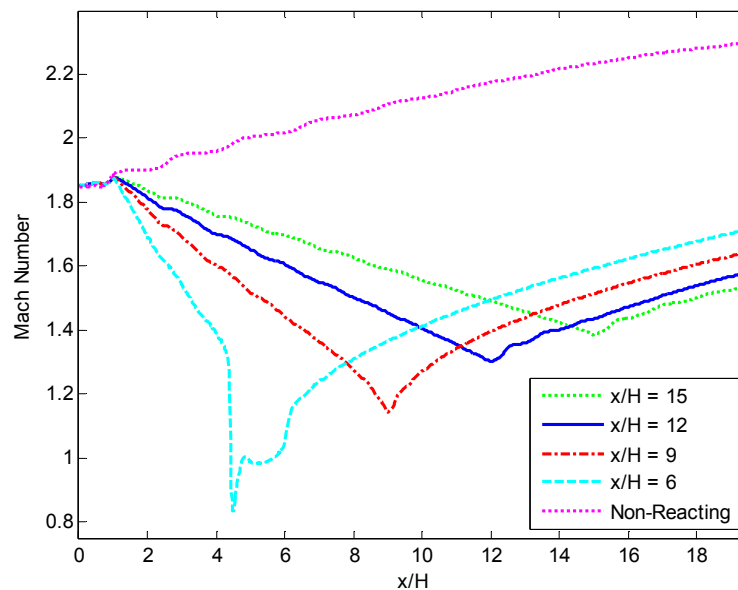
(b) Mach number along centerline of simplified combustor.

Figure 5.15: Simulated pressure along the top wall (*a*) and Mach number along the centerline (*b*) for the supersonic combustion, simplified combustor model with Φ = 0.11.

55

flow field.

   As proposed, the shorter the heat release domain, the higher the chance of thermal choking. This is proven in Figure 5.15, as well as in the simulation results shown in Figure 5.16. For all cases in which the heat release domain ended at $x/H = 9$ or higher, the flow remained supersonic. However, for the case ending at $x/H = 6$, the flow was thermally choked. This is evident in Figure 5.15 (b) when the Mach number is reduced to approximately 0.8 just after $x/H = 4$. When the flow is thermally choked,
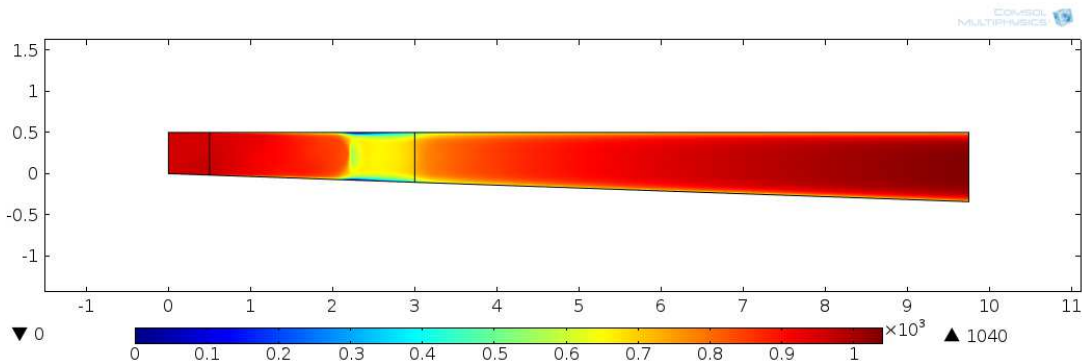
(a) Heat release domain from $x/H = 1$ to $x/H = 6$. Flow is thermally choked.
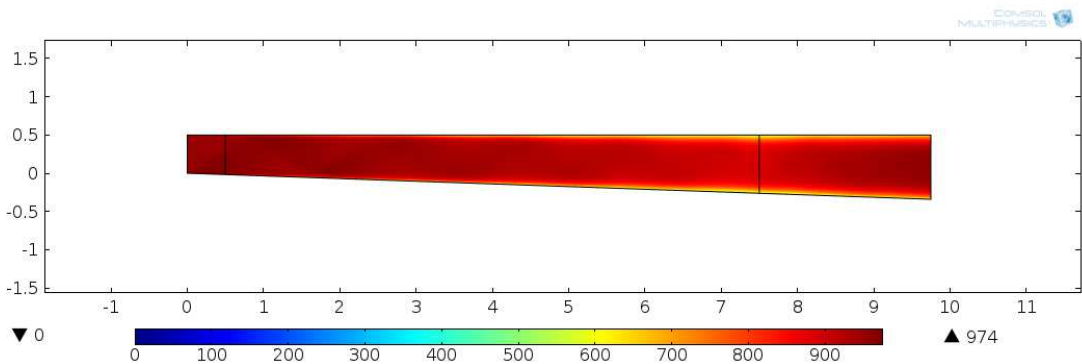
(b) Heat release domain from $x/H = 1$ to $x/H = 15$ as shown in Figure 5.6 (c). Flow remains supersonic as evident in Figure 5.15 (b).

Figure 5.16: Velocity surface plots for thermally choked (a) and supersonic (b) simplified combustor simulations. Units are in m/s.

56

a normal shock forms to decelerate the flow. This normal shock causes a sharp rise in static pressure which is shown in Figure 5.15 (a).

A non-reacting simulation was also run and the results are compared in Figure 5.15. This allows for the verification that the heat release is actually able to overcome the effect of area divergence for this particular setup. As expected for area divergence only, the Mach number accelerates, simultaneously lowering the static pressure. This can be proven using the following relation [38].

$$\frac{du}{u} = \frac{-\dfrac{dA}{A}}{1 - M^2} \tag{5.1}$$

In cases where the flow is supersonic, the term $1 - M^2$ is negative and it is found that increasing the area causes an increase in velocity and thus the Mach number [38]. Similarly, the change due to heat addition can also be calculated using a series of two equations. These are found in [27].

$$q = c_p\left(T_{o_2} - T_{o_1}\right) \tag{5.2}$$

$$\frac{T_{o_2}}{T_{o_1}} = \left(\frac{1 + \gamma M_1^2}{1 + \gamma M_2^2}\right)^2 \left(\frac{M_2}{M_1}\right)^2 \left(\frac{1 + \dfrac{\gamma - 1}{2}M_2^2}{1 + \dfrac{\gamma - 1}{2}M_1^2}\right) \tag{5.3}$$

If the amount of heat added to the system and the initial conditions are known, equations (5.2-5.3) can be used to calculate a very rough estimate of the final Mach number. However, this does not take into account the effects of mass injection, friction, or change in molecular weight. In order to calculate a more accurate result that takes some or all of these parameters into account, the influence coefficients for quasi-one-dimensional flow must be used. This forms a differential equation that must be solved rather than an algebraic one such as equation (5.3). These coefficients as well as more

57

detailed information about the effects of Rayleigh flow or area expansion can be found in *Shapiro* [37] and Appendix 3.

5.4.3. Simplified Supersonic Combustion Case w/ Wall-Normal Fluctuations

Next, the effect of the heat release fluctuating in the wall-normal direction was tested. This would simulate the flame traversing from the upper to the lower portion of the combustor or vice versa. The heat release domain was based on the size as shown in Figure 5.6, but only covered half of the geometry from the centerline to the top or bottom wall. This is shown in Figure 5.17. The maximum available amount of heat release was used for all cases. Also, the inlet conditions are the same as what was used for all of the supersonic combustion cases in section 5.4.2. There was no cavity or fuel injection present in these models in order to test the effect of heat release only. This helps investigate another mechanism that can be found in a real-world, time-dependent combustion zone.
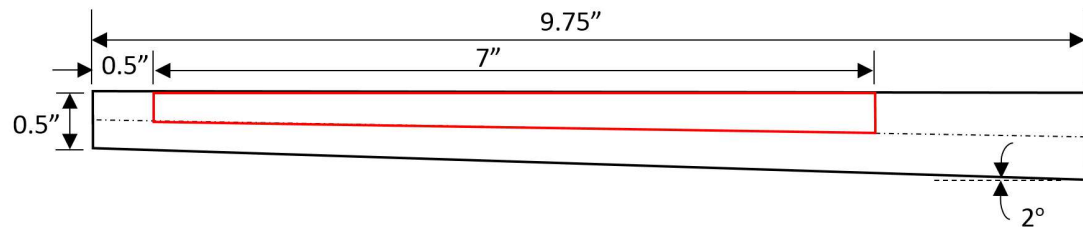
Figure 5.17: Simplified combustor geometry with heat release domain on upper half of geometry. Dashed line represents the centerline between the top and bottom walls. Same total amount of heat release as before.

When the results were plotted, it was observed that the heat release in the upper and lower portions of the combustor produced pressure profiles along the top wall that were the equivalent of being 180 *degrees* out of phase. In other words, the local maxima of one curve corresponded with the local minima of the other. To test the effect of the

58
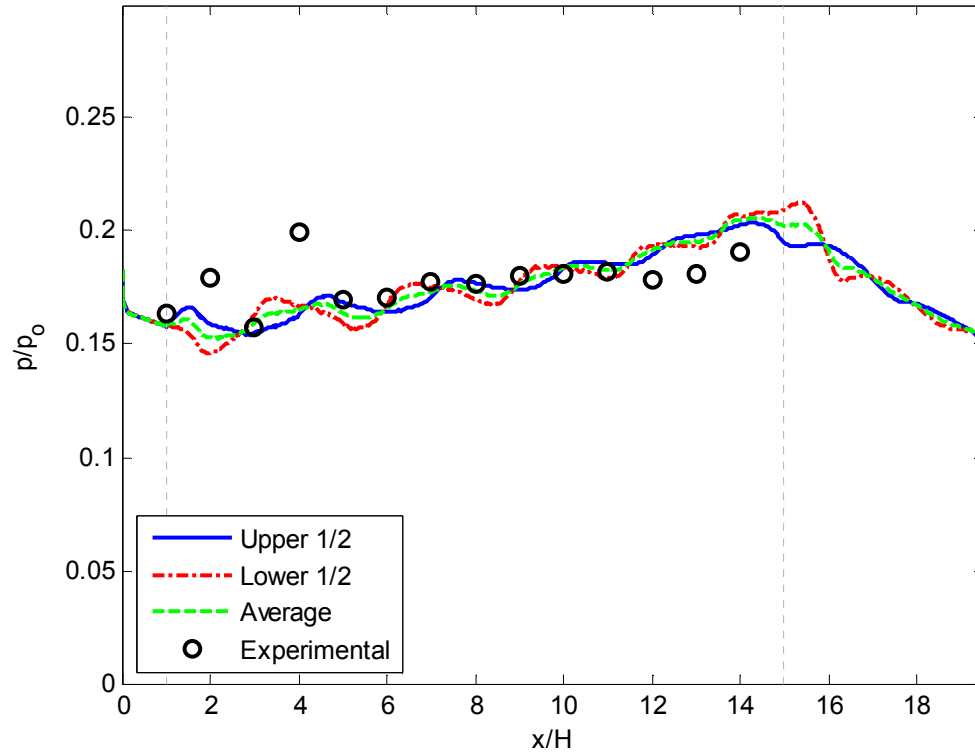
Figure 5.18: Static pressure along top wall of simplified combustor, supersonic combustion case for $\Phi = 0.11$. Heat release domain between centerline and upper or lower wall from $x/H = 1$ to 15. Average value between upper and lower curves is also plotted. Experimental data from [1].

flame oscillating in this manner, the average of these two curves was also found and is plotted in Figure 5.18 for comparison.

Also shown in Figure 5.19 are the temperature surface plots for the upper and lower half simulations. This simplified geometry is a far cry from the 3-D geometry with the cavity that was found in the experimental setup. However, to see the data match so closely helps prove the feasibility of using the COMSOL Multiphysics framework for modeling the internal flow field of a scramjet engine. A more accurate result could possibly be obtained using a 3-D time-dependent solution with a chemically reacting model. In this situation, the purpose was to see the effect that

59

changing certain parameters such as intensity or location would have on the results. This also provides a better solution than using a 1-D model for heat release because it takes into account any pseudo-shock waves that might be present. These are evident in the simulation results whenever the pressure fluctuates about the experimental results.
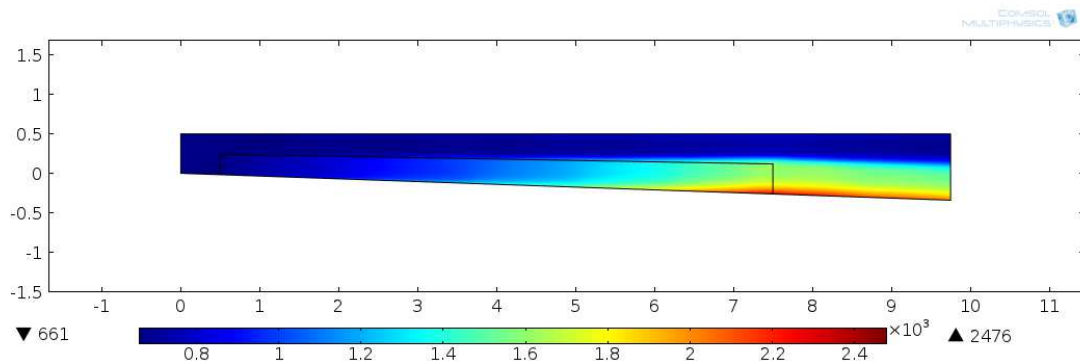
(a) Simplified combustor with heat release on lower half.
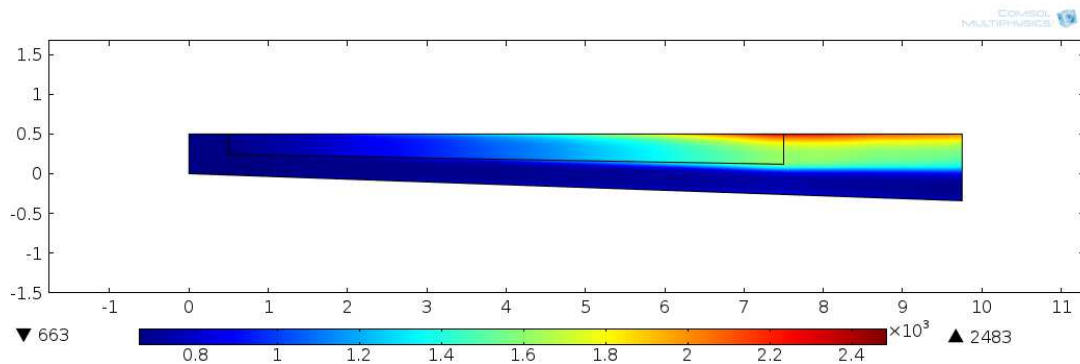
(b) Simplified combustor with heat release on upper half.

Figure 5.19: Temperature surface plots for lower (a) and upper (b) half of simplified combustor model. Heat release between $x/H = 1$ and $x/H = 15$. Units in K.

5.5. Performance Comparison

One of the advantages of CFD simulations is that the estimated flow properties are known over the entire domain rather than at distinct points along a surface like the experimental measurements. This allows for a comparison of performance parameters such as thrust over a wide range of conditions. This was calculated by integrating over the exit plane of the combustor to find the thrust per unit width.

$$\tau = \int_{Exit} (P + \rho u^2) \, dy \qquad (5.4)$$

The thrust was calculated for non-reacting, supersonic combustion, and thermally choked cases for both the cavity combustor and the simplified geometry. This allowed for the comparison of the mode of operation on performance and gave an insight into the drag penalty caused by the cavity. The inlet conditions were the same for all cases shown in Figure 5.20 and Table 5.1.

Another condition that was compared for each of the six cases was the maximum wall temperature. This is important for several main regions of interest: material limitations and thermal protection system requirements. As seen in Chapter 2 of *MIL-HDBK-5H,* material properties can rapidly degrade as a function of temperature [39]. This is very undesirable as it can compromise the vehicle's structural integrity or even cause a loss of the vehicle altogether. If the design calls for operating temperatures above these limitations, a thermal protection system must be installed to insulate or protect the materials to prevent compromising or failure of the structure. The maximum temperatures found in the simulations give an insight into and basic comparison of the conditions that could be expected during dual-mode scramjet operation.

www.manaraa.com
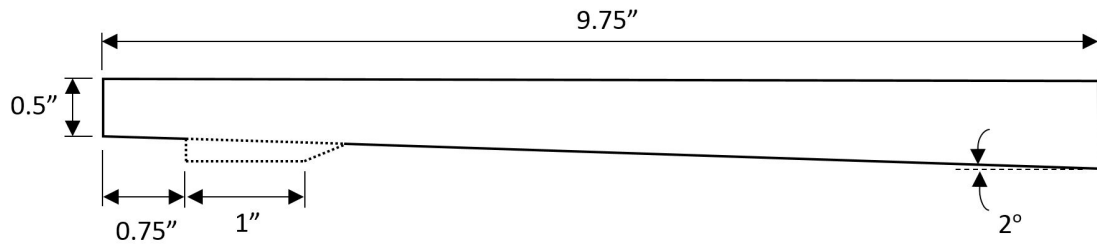
(a) Simplified (no cavity) and cavity combustors with no heat release for non-reacting flow comparison.
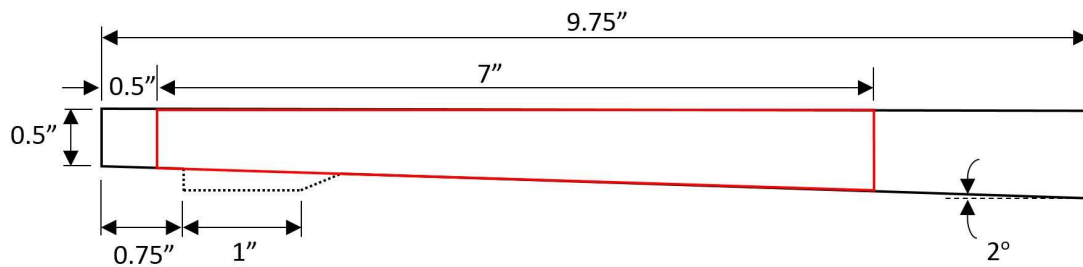
(b) Simplified and cavity combustors under supersonic combustion mode.
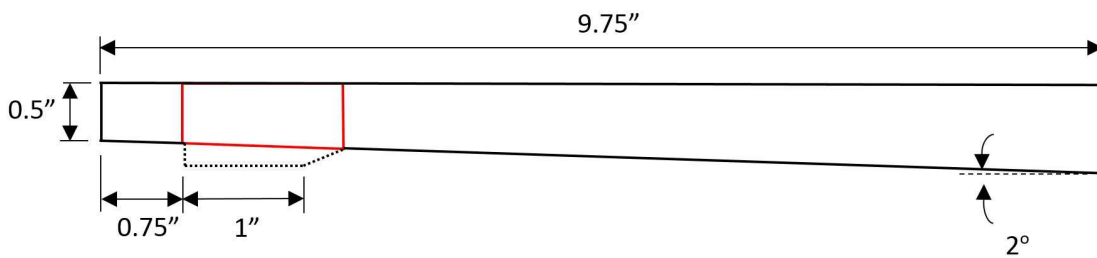
(c) Simplified and cavity combustors under thermally choked combustion mode.

Figure 5.20: Diagram showing both simplified geometry (no cavity) and cavity combustor with corresponding heat release domain used for each mode of operation.

As mentioned previously, the same inlet conditions were used for all six cases. In addition, the same total amount of heat release was added for the four reacting flow cases. However, due to the difference in area of the heat release domains for the supersonic combustion and thermally choked cases shown in Figure 5.20 (b) and (c) respectively, the heat release density was not the same between different combustion modes. The numerical results are provided in Table 5.1 for comparison.

62

Table 5.1: Thrust estimation for non-reacting, supersonic combustion, and thermally choked modes of operation.

Combustor Geometry	Mode of Operation	Thrust per unit width, τ (N/m)
Simplified	Non-Reacting	8152
	Supersonic	8545
	Thermally Choked	8829
Cavity	Non-Reacting	7855
	Supersonic	8420
	Thermally Choked	8686

As shown in Table 5.1, higher thrust is produced if the engine is thermally choked than if it operates under supersonic combustion mode due to the increase in pressure caused from choking the flow. The cavity produces the largest amount of drag for the non-reacting case than for any other mode of operation shown. The difference in thrust produced for the supersonic and thermally choked cases is only about 50% as much as for the non-reacting case, showing that the cavity had much less of an impact for a reacting case, regardless of the mode of combustion. The effect of the cavity was the least for the supersonic mode of operation, producing little drag as shown in Table 5.2. However, the effect of mode of operation on wall temperature must also be taken into account. This will be presented later in Table 5.3.

Table 5.2: Effect of cavity and mode of operation on performance characteristics. Differences were calculated between the cavity and simple combustor results from Table 5.1. Negative thrust denotes drag.

Mode of Operation	$\Delta\tau$ (N/m)
Non-Reacting	-297
Supersonic	-125
Thermally Choked	-143

To better understand the effect of the cavity, it is easier to see the results visually. Presented in Figure 5.21 is a bar graph comparing the simplified and cavity combustor cases for all three modes of operation that were simulated. It can easily be seen that the thermally choked case produced the highest thrust for both geometries that were simulated. It is also clear both in Table 5.2 and Figure 5.21 that the cavity had the greatest drag penalty compared to the other two modes of operation.
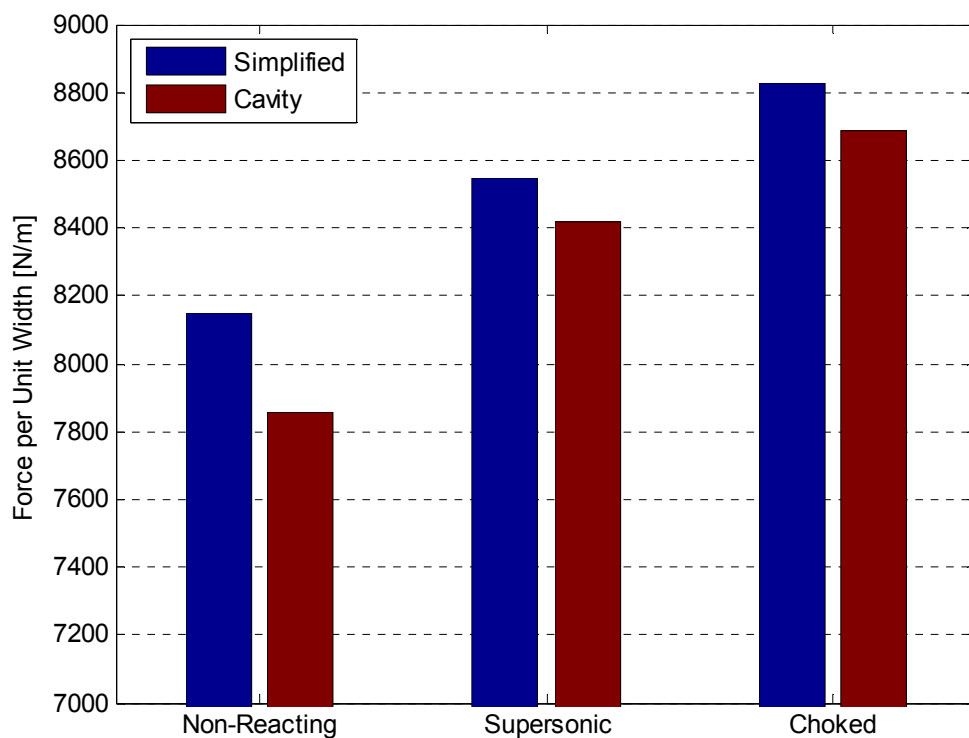
Figure 5.21: Comparison of thrust produced by simplified or cavity combustor geometries under various modes of operation.

One result of interest is that the wall temperature is virtually the same whether a cavity is present or not for a non-reacting case. On the contrary, the difference between the supersonic and thermally choked cases are much more profound. As expected, thermally choking the flow greatly increases the temperature due to the strong shock

64

that can form. This is shown numerically in Table 5.3 with a visual comparison following in Figure 5.22. However, as seen in Table 5.3, the presence of a cavity can actually lessen the effect of thermal choking on the wall temperature. Velocity surface plots for the cases shown in Table 5.3 below can be found in Figure 5.23.

Table 5.3: Effect of mode of operation on maximum wall temperature.

Combustor Geometry	Mode of Operation	Maximum Static Wall Temperature (K)	$\Delta T_{max} = T_{choked} - T_{s.s.}$ (K)
Simplified	Supersonic	1416	410
	Thermally Choked	1826	
Cavity	Supersonic	1405	275
	Thermally Choked	1680	
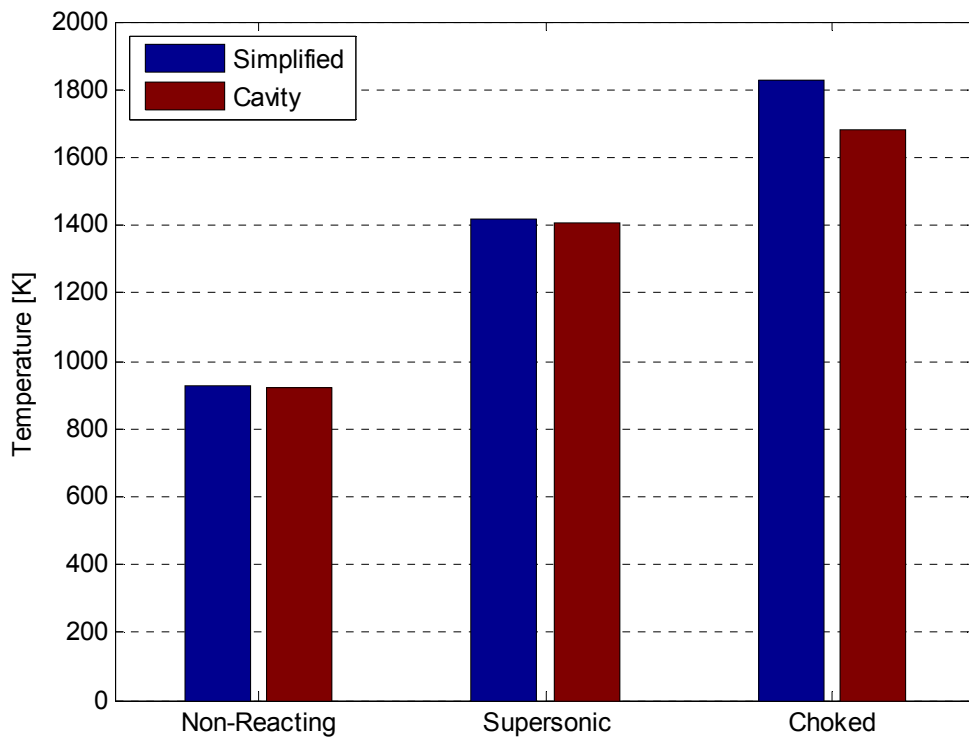
Figure 5.22: Comparison of maximum wall temperature for simplified and cavity combustor geometries while under various modes of operation.

65

The desired mode of operation is not as simple as looking at two performance parameters. While they are important, many more considerations must be taken into account such as weight, cost, and flight regime. In the particular cases that were simulated, the Mach number was rather low for a typical scramjet engine. If the Mach number were to be increased, the effect of thermal choking becomes much larger, often to the point that supersonic combustion is the only viable option. While there might exist a material that can withstand the extreme temperatures in those cases, its weight or cost might be prohibitive to the point that they cannot be used in the engine design.

It is also worth noting that the cases simulated here can apply to a more general dual-mode scramjet geometry that contains a cavity. While the dimensions and inlet conditions were based on those that were used during the experiments by *Aguilera* [1], the results that were found are more general in nature. Although the numbers will vary, the general trends that were seen could apply over a broader range of conditions. The exact results will be based on the cavity geometry, heat release location, and flight Mach number of the engine.
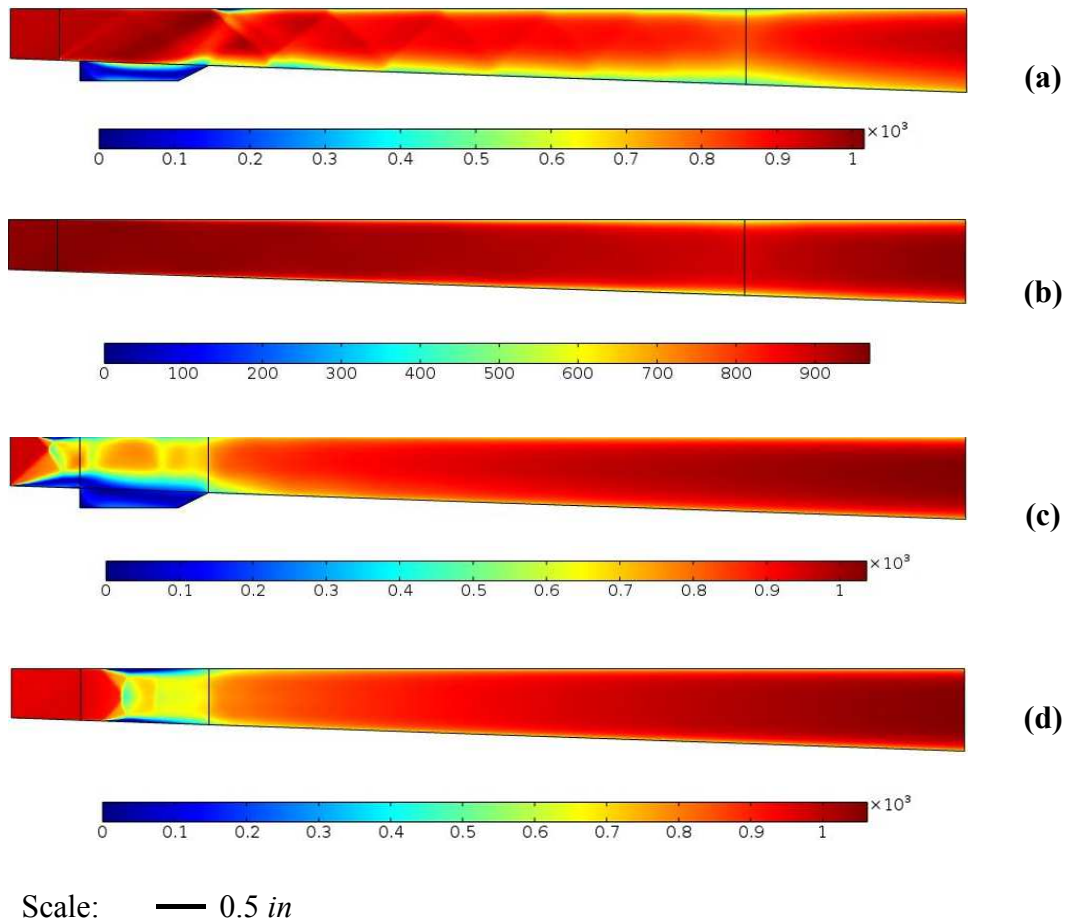
Figure 5.23: Velocity surface plots for cavity geometry and simplified case for supersonic combustion (*a,b*) and thermally choked cases (*c,d*). Total amount of heat release, inlet conditions, and overall geometry are the same for all. Only the cavity is added for (*a,c*) and heat release intensity varies between the supersonic and thermally choked cases. Units in *m/s*.

Chapter 6: Summary and Conclusions

6.1. Summary of Major Results and Important Findings

6.1.1. Simulation Summary

A dual-mode scramjet engine was broken into two distinct components for simulation purposes in order to decrease computational cost and allow for the focus of the research to remain on the effect of combustor heat release. The isolator was modeled for all combustor equivalence ratios and the backpressure was matched for each through the generation of a normal shock train structure. As expected, the shock train structure propagated upstream as the backpressure values were increased.

The combustor was modeled with conditions based on those from the experiments before a series of parametric sweeps for heat release location and intensity. Location was varied both streamwise and transversely while keeping all other conditions constant. Simulations were conducted for both supersonic combustion mode and thermally choked mode of operation allowing for both a qualitative and quantitative comparison of performance characteristics. Thrust performance and thermal protection system requirements were compared under various modes of operation and the effect caused by the presence of a wall cavity was seen. As will be further explained in the next section, the presence of a cavity caused both the drag penalty and thermal protection system need to decrease during operation with heat addition in comparison to a non-reacting case.

68

6.1.2. Important Results and Findings

The major results and findings presented in this research are presented below.

- Developed a computational framework using the COMSOL Multiphysics® platform to simulate a dual-mode scramjet isolator-combustor flow field and analyzed the thrust potential for various combustion mode operation

- Matched backpressure ratio of isolator for all combustor equivalence ratios through the generation of a normal shock train; although an oblique shock structure was seen in experiments, it was shown that COMSOL was capable of generating these flow features

- Demonstrated a deduction technique to approximate the heat release distribution from the wall pressure data that was obtained experimentally

- Simulated the experimental data under both thermally choked and supersonic combustion modes of operation and studied the effects of combustion most on thrust potential and maximum wall temperature

- Evaluated the amount of thrust loss associated with the presence of a wall cavity for flame holding under different combustion mode operation

  o The amount of thrust loss due to cavity-induced drag decreased substantially with combustion. Specifically, the cavity drag caused 3.64% loss of propulsive force in the non-reacting flows ($\Phi = 0$), but this loss was reduced to 1.62% when thermally choked and 1.46% for supersonic combustion ($\Phi = 0.12$)

- Assessed the quantitative tradeoffs between thrust and thermal protection need for two selected cases

69

- o The simplified combustor geometry produced a thrust increase of 3.31% when operating under thermally choked mode instead of supersonic combustion. However, this also produces a 29.0% increase in maximum wall temperature

  o The cavity geometry produced an increase of 3.16% in thrust when the flow is thermally choked rather than under supersonic combustion mode, but maximum wall temperature increases 19.6% as a result

- Compared the thermal protection system requirements with and without the presence of a cavity

  o The presence of a wall cavity was shown to reduce the maximum wall temperature 0.78% under supersonic operation and 8.00% under thermally choked mode. Therefore, not only does the cavity aid in flame holding to allow supersonic combustion, it also aids in reducing the maximum wall temperature seen during operation, independent of combustion mode.

  o For the non-reacting case, the effect of the cavity only decreased the maximum wall temperature by a virtually negligible 0.11% from 924 K to 923 K.

6.2. Academic Contribution

This research contributed to the field of hypersonic airbreathing propulsion by:

- Showing that it is possible to find a balance between Rayleigh flow and area expansion within a typical dual-mode scramjet operating regime such that static wall pressure increases while the flow is expanding

70

- Analyzing the effect of heat release location on the overall flow field by parametrically changing the intensity and location of a heat release domain

- Quantitatively analyzing the effect on performance parameters caused by the presence of a wall cavity and combustor operation mode such as propulsive force and thermal protection system requirements

6.3. Recommendations for Future Work

Below are several topics that could be addressed in order to further expand and refine the computational framework that was established with this research.

- In order to more accurately simulate the model scramjet, there are two main revisions that could have a large effect on the results:

    o The model could be greatly improved if simulated in 3-D space, rather than the 2-D that was used here. This would enable the visualization of the three-dimensionality of the flow structures as they exist in the experiments. However, this would likely require a drastic increase in computational power.

    o In order to have a much more accurate representation of the combustion reaction, a full chemically reacting model would be necessary. This would greatly improve the accuracy of the location of heat addition based on fuel-air mixing and would not limit the model to having a constant heat release density over a set domain.

    o Additionally, for full modeling of the experimental dual-mode scramjet setup, a time dependent study could be run in place of the stationary ones used herein. This would help visualize and fluctuations that occur

71

in the flame structure or location and should produce a time-averaged pressure curve as recorded by *Aguilera* [1].

- In order to try to match the isolator shock train structure more closely, the boundary layer formation in the isolator should be altered to better reflect the experiments. Rather than modeling the nozzle block that was located upstream of the isolator, only the isolator itself was modeled for the purpose of this research. This means that these models do not take into account the initial thickness of the boundary layer that has already formed before the flow enters the isolator duct.

Appendices

Table A1.1: Computer hardware and software specifications.

Component	Details
Manufacturer	Dell
Model	Precision M6800 Mobile Workstation
Processor	Intel Core i7-4390MX; Quad Core Extreme; 3.00 GHz (3.9 GHz Turbo)
Operating System	Windows 7 Professional 64 Bit
Video Card	Nvidia Quadro K4100M with 4 GB GDDR5
Memory	32 GB (4x8 GB) 1600 MHz DDR3
Hard Drive	1 TB Hybrid with 8 GB SSD Flash
Operating System	Windows 7 Professional SP1 (64-bit)
COMSOL Multiphysics	Version 4.4.0.248

Table A1.2: Mesh convergence study run times for $\Phi = 0.12$.

Mesh	Study	Degrees of Freedom (plus internal DOF)	Solution Time	Auxiliary Sweep Parameters
Coarse	Study 1 – Slip	28836 (512 int.)	36 s (0:36)	
	Study 2 – Wall Functions	80698 (974 int.)	642 s (10:42)	1000,100,10,1
	Study 3 – No Slip	132330 (1230 int.)	1905 s (31:45)	
Normal	Study 1 – Slip	62250 (762 int.)	94 s (01:34)	
	Study 2 – Wall Functions	132484 (1214 int.)	1238 s (2038)	1000,100,10,1
	Study 3 – No Slip	300105 (2580 int.)	8727 s (02:25:27)	
Fine	Study 1 – Slip	101742 (976 int.)	165 s (02:45)	
	Study 2 – Wall Functions	303408 (2564 int.)	3327 s (55:27)	1000,100,10,1
	Study 3 – No Slip	656350 (4942 int.)	13977 s (03:52:57)	

Table A1.3: Isolator simulation run times for all Φ values.

Equivalence Ratio	Study	Degrees of Freedom (plus internal DOF)	Solution Time	Auxiliary Sweep Parameters
Φ = 0.00	Study 1 – Slip	62250 (762 int.)	92 s (01:32)	1000,100,10,1
	Study 2 – Wall Functions	132484 (1214 int.)	323 s (05:23)	1000,100,10,1
	Study 3 – No Slip	300105 (2580 int.)	1264 s (21:04)	100,10,1
Φ = 0.04	Study 1 – Slip	62250 (762 int.)	92 s (01:32)	1000,100,10,1
	Study 2 – Wall Functions	132484 (1214 int.)	293 s (04:53)	1000,100,10,1
	Study 3 – No Slip	300105 (2580 int.)	1289 s (21:29)	100,10,1
Φ = 0.08	Study 1 – Slip	62250 (762 int.)	86 s (01:26)	1000,100,10,1
	Study 2 – Wall Functions	132484 (1214 int.)	294 s (04:54)	1000,100,10,1
	Study 3 – No Slip	300105 (2580 int.)	1214 s (20:14)	100,10,1
Φ = 0.12	Study 1 – Slip	62250 (762 int.)	94 s (01:34)	1000,100,10,1
	Study 2 – Wall Functions	132484 (1214 int.)	1238 s (20:38)	1000,100,10,1
	Study 3 – No Slip	300105 (2580 int.)	8727 s (02:25:27)	100,10,1
Φ = 0.16	Study 1 – Slip	62250 (762 int.)	95 s (01:35)	1000,100,10,1
	Study 2 – Wall Functions	132484 (1214 int.)	1436 s (23:56)	1000,100,10,1
	Study 3 – No Slip	300105 (2580 int.)	19423 s (05:23:43)	100,10,1
Φ = 0.20	Study 1 – Slip	62250 (762 int.)	88 s (01:28)	1000,100,10,1
	Study 2 – Wall Functions	132484 (1214 int.)	1523 s (25:23)	1000,100,10,1
	Study 3 – No Slip	300105 (2580 int.)	7933 s (02:12:13)	100,10,1

Table A1.4: Cavity combustor with varying inlet conditions run times for $\Phi = 0.12$.

Inlet Pressure (*kPa*)	Study	Degrees of Freedom (plus internal DOF)	Solution Time	Auxiliary Sweep Parameters
207.6	Study 1 – Slip	38034 (643 int.)	630 *s* (10:30)	1000,100,10,1
	Study 2 – Wall Functions	89515 (1047 int.)	1447 *s* (24:07)	1000,100,10,1
	Study 3 – No Slip	207925 (2131 int.)	3099 *s* (51:39)	100,10,1
150	Study 1 – Slip	38034 (643 int.)	196 *s* (3:16)	1000,100,10,1
	Study 2 – Wall Functions	89515 (1047 int.)	540 *s* (9:00)	1000,100,10,1
	Study 3 – No Slip	207925 (2131 int.)	3487 *s* (58:07)	100,10,1
145	Study 1 – Slip	38034 (643 int.)	192 *s* (3:12)	1000,100,10,1
	Study 2 – Wall Functions	89515 (1047 int.)	558 *s* (9:18)	1000,100,10,1
	Study 3 – No Slip	207925 (2131 int.)	3522 *s* (58:42)	100,10,1
135	Study 1 – Slip	38034 (643 int.)	203 *s* (3:23)	1000,100,10,1
	Study 2 – Wall Functions	89515 (1047 int.)	566 *s* (9:26)	1000,100,10,1
	Study 3 – No Slip	207925 (2131 int.)	3863 *s* (1:04:23)	100,10,1

Table A1.5: Cavity combustor with varying heat release domain location run times for $\Phi = 0.12$.

Heat Release Domain Location	Study	Degrees of Freedom (plus internal DOF)	Solution Time	Auxiliary Sweep Parameters
Full Cavity	Study 1 – Slip	38034 (643 int.)	203 *s* (3:23)	1000,100,10,1
	Study 2 – Wall Functions	89515 (1047 int.)	566 *s* (9:26)	1000,100,10,1
	Study 3 – No Slip	207925 (2131 int.)	3863 *s* (1:04:23)	100,10,1
Lower 1/2 Cavity	Study 1 – Slip	38346 (684 int.)	538 *s* (8:58)	1000,100,10,1
	Study 2 – Wall Functions	89516 (1020 int.)	1469 *s* (24:29)	1000,100,10,1
	Study 3 – No Slip	207870 (2131 int.)	3170 *s* (52:50)	100,10,1
Upper 1/2 Cavity	Study 1 – Slip	38304 (697 int.)	248 *s* (4:08)	1000,100,10,1
	Study 2 – Wall Functions	88369 (1077 int.)	733 *s* (12:13)	1000,100,10,1
	Study 3 – No Slip	207465 (2149 int.)	2824 *s* (47:04)	100,10,1

Table A1.6: Simplified combustor with varying heat release run times for $\Phi = 0.12$.

Heat Release	Study	Degrees of Freedom (plus internal DOF)	Solution Time	Auxiliary Sweep Parameters
Non-Reacting	Study 1 – Slip	36606 (631 int.)	77 s (1:17)	
	Study 2 – Wall Functions	84769 (1016 int.)	590 s (9:50)	1000,100,10,1
	Study 3 – No Slip	200495 (2094 int.)	2387 s (39:47)	
1/2 LHV	Study 1 – Slip	36690 (636 int.)	50 s (0:50)	
	Study 2 – Wall Functions	84990 (1020 int.)	614 s (10:14)	1000,100,10,1
	Study 3 – No Slip	200735 (2100 int.)	3578 s (59:38)	
2/3 LHV	Study 1 – Slip	36690 (636 int.)	60 s (1:00)	
	Study 2 – Wall Functions	84990 (1020 int.)	632 s (10:32)	1000,100,10,1
	Study 3 – No Slip	200735 (2100 int.)	3872 s (1:04:32)	
Full LHV	Study 1 – Slip	36690 (636 int.)	78 s (1:18)	
	Study 2 – Wall Functions	84990 (1020 int.)	1300 s (21:40)	1000,100,10,1
	Study 3 – No Slip	200735 (2100 int.)	4266 s (1:11:06)	

Table A1.7: Simplified combustor run times for $\Phi = 0.11$. In all cases, the maximum amount of heat release was used over a simple trapezoidal domain that extended from x/H = 1 to x/H = 15.

Heat Release Domain	Study	Degrees of Freedom (plus internal DOF)	Solution Time	Auxiliary Sweep Parameters
Top to Bottom Wall	Study 1 – Slip	36690 (636 int.)	78 s (01:18)	
	Study 2 – Wall Functions	84990 (1020 int.)	1360 s (22:40)	1000,100,10,1
	Study 3 – No Slip	200735 (2100 int.)	4584 s (01:16:24)	
Centerline to Bottom Wall	Study 1 – Slip	37158 (973 int.)	78 s (01:18)	
	Study 2 – Wall Functions	79703 (1333 int.)	1305 s (21:45)	1000,100,10,1
	Study 3 – No Slip	193535 (2479 int.)	4669 s (01:17:49)	
Centerline to Top Wall	Study 1 – Slip	37056 (972 int.)	79 s (01:19)	
	Study 2 – Wall Functions	79655 (1333 int.)	1368 s (22:48)	1000,100,10,1
	Study 3 – No Slip	193730 (2479 int.)	5307 s (01:28:27)	

Table A1.8: Simplified combustor run times for $\Phi = 0.11$. In all cases, the maximum amount of heat release was used over a simple trapezoidal domain that extended from x/H = 1 to between x/H = 6 and x/H = 15.

Heat Release Ending Location	Study	Degrees of Freedom (plus internal DOF)	Solution Time	Auxiliary Sweep Parameters
x/H = 6	Study 1 – Slip	36612 (627 int.)	103 *s* (01:43)	
	Study 2 – Wall Functions	85088 (1014 int.)	1514 *s* (25:14)	1000,100,10,1
	Study 3 – No Slip	201155 (2090 int.)	4051 *s* (01:07:31)	
x/H = 9	Study 1 – Slip	36618 (631 int.)	91 *s* (01:31)	
	Study 2 – Wall Functions	85508 (1018 int.)	1474 *s* (24:34)	1000,100,10,1
	Study 3 – No Slip	200565 (2092 int.)	4717 *s* (01:18:37)	
x/H = 12	Study 1 – Slip	36810 (635 int.)	86 *s* (01:26)	
	Study 2 – Wall Functions	84360 (1018 int.)	1374 *s* (22:54)	1000,100,10,1
	Study 3 – No Slip	200875 (2097 int.)	6851 *s* (01:54:11)	
x/H = 15	Study 1 – Slip	36690 (636 int.)	78 *s* (01:18)	
	Study 2 – Wall Functions	84990 (1020 int.)	1360 *s* (22:40)	1000,100,10,1
	Study 3 – No Slip	200735 (2100 int.)	4584 *s* (01:16:24)	

A2. Derivation of Heat Release Value

In the case of the simulations that were completed, the three-dimensional values from the experiments had to be converted to their equivalent two-dimensional counterparts in order to estimate the amount of heat that was released. The first step was to find the equivalent dimensions to transform the circular fuel injection orifice into a two-dimensional slot that extends across the entire span of the scramjet that has the same injection area, A_{inj}. A diagram of this can be seen in Figure A2.1 below. Note that the fin is only there for illustrative purposes as the fin itself was not modeled.
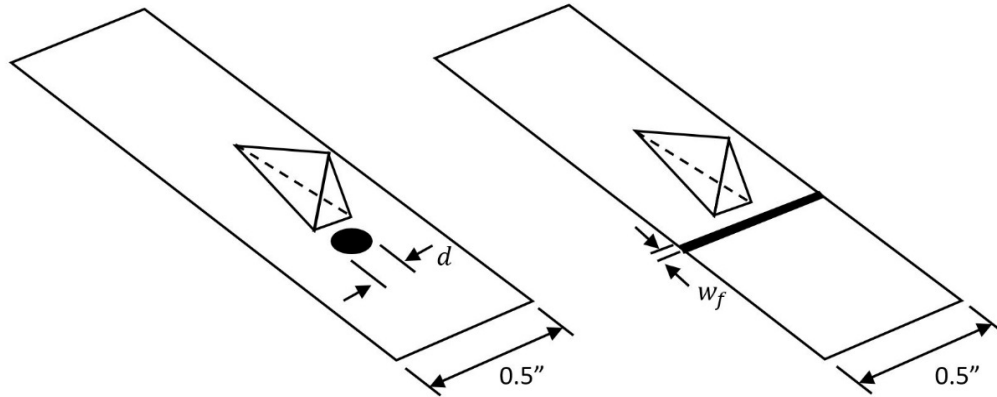
Figure A2.1: Comparison of original fuel injection orifice (*left*) to fuel injection slot of same area (*right*). *Portion of diagram (left) adapted by author from* [1].

Using the relation from Appendix II of *Hill and Peterson* [40], the specific heat capacity at constant pressure of hydrogen gas was calculated.

$$C_p = 56.505 - 702.74\beta^{-0.75} + 1165.0\beta^{-1} -$$

$$560.70\beta^{-1.5} \left[\frac{kJ}{kmol \cdot K}\right] \tag{A2.1}$$

Where

$$\beta = T(K)/100$$

The relation shown in equation (A2.1) is valid for temperatures of 300-3500 K. The temperature was substituted into equation (A2.1) and C_p was multiplied by the molecular weight of the gas. Using this value and the following equation, the ratio of specific heats was calculated.

$$C_p = \frac{\gamma R}{\gamma - 1}$$ (A2.2)

For any given combustor equivalence ratio and fuel mass flow rate values, the fuel mass flow rate per unit length can be found as:

$$\dot{m}_{f_{2D}} = \frac{\dot{m}_{f_{3D}}}{A_{inj}} w_f \left[\frac{(kg/s)}{m} \right]$$ (A2.3)

Assuming standard temperature and pressure, the ideal gas law and mass flow rate are then employed to calculate the incoming Mach number of the fuel. The maximum heat release value that is expected from a given amount of fuel is then calculated. The heat of reaction of hydrogen fuel is 120 *MJ/kg fuel* [4]. COMSOL requires the units of *W/m³* for defining volumetric heat release over a domain. In the case of these two-dimensional simulations, a unit depth of 1 *m* is assumed.

$$Q_{max} = \frac{h_{pr} \dot{m}_{f_{2D}}}{A_{HR}}$$ (A2.4)

This provides the highest amount of heat release that is possible for a given fuel mass flow rate into the model scramjet. Any amount of heat release up to this limiting case is acceptable, so long as the simulations do not exceed this value.

Table A2.1: Maximum Heat Release Values for Simulated Cases

Φ	$\dot{m}_{f_{2D}}$ (g/s)/m	$Q_{max} A_{HR}$ kW/m
B 0.117	25.3	3033
F 0.114	24.5	2938
F 0.193	41.6	4989

82

A3. Influence Coefficients for Quasi One-Dimensional Flow

Shapiro presents the following system of equations that can be used to calculate the changes in thermodynamic or flow parameters due to a change in area, mass injection, heat addition, and more [37]. The effect of each can be calculated individually or a partial differential equation can be derived that takes many variations into account. As an example, use the system of equations presented on the following page to calculate the change in Mach number due to area divergence, heat release, and fuel injection only. This gives equation A3.1 below. As seen on the following page, other parameters could be taken into account such as work, wall friction, and more.

$$\frac{dM^2}{M^2} = -\frac{2\left(1 + \frac{\gamma - 1}{2}M^2\right)}{1 - M^2}\frac{dA}{A} + \frac{1 + \gamma M^2}{1 - M^2}\frac{dQ}{C_p T}$$

$$-2\frac{\gamma M^2\left(1 + \frac{\gamma - 1}{2}M^2\right)}{1 - M^2}\frac{u_g}{u}\frac{d\dot{m}}{\dot{m}}$$

(A3.1)

A similar process can be followed to find the change in properties such as velocity, temperature, and pressure.

Influence coefficients for quasi one-dimensional flow as presented in *Shapiro* [37].

$$
\begin{bmatrix} \dfrac{dM^2}{M^2} \\[6pt] \dfrac{du}{u} \\[6pt] \dfrac{da}{a} \\[6pt] \dfrac{dT}{T} \\[6pt] \dfrac{d\rho}{\rho} \\[6pt] \dfrac{dp}{p} \\[6pt] \dfrac{dF}{F} \\[6pt] \dfrac{ds}{C_p} \end{bmatrix}
=
\begin{bmatrix}
-\dfrac{2\left(1+\frac{\gamma-1}{2}M^2\right)}{1-M^2} & \dfrac{1+\gamma M^2}{1-M^2} & \dfrac{\gamma M^2\left(1+\frac{\gamma-1}{2}M^2\right)}{1-M^2} & \dfrac{2(1+\gamma M^2)\left(1+\frac{\gamma-1}{2}M^2\right)}{1-M^2} & -\dfrac{1+\gamma M^2}{1-M^2} & -1 \\[12pt]
-\dfrac{1}{1-M^2} & \dfrac{1}{1-M^2} & \dfrac{\gamma M^2}{2(1-M^2)} & \dfrac{1+\gamma M^2}{1-M^2} & -\dfrac{1}{1-M^2} & 0 \\[12pt]
\dfrac{\frac{\gamma-1}{2}M^2}{1-M^2} & \dfrac{1-\gamma M^2}{2(1-M^2)} & -\dfrac{\gamma(\gamma-1)M^4}{4(1-M^2)} & -\dfrac{\frac{\gamma-1}{2}M^2(1+\gamma M^2)}{1-M^2} & \dfrac{\gamma M^2-1}{2(1-M^2)} & \dfrac{1}{2} \\[12pt]
\dfrac{(\gamma-1)M^2}{1-M^2} & \dfrac{1-\gamma M^2}{1-M^2} & -\dfrac{\gamma(\gamma-1)M^4}{2(1-M^2)} & -\dfrac{(\gamma-1)M^2(1+\gamma M^2)}{1-M^2} & \dfrac{(\gamma-1)M^2}{1-M^2} & 0 \\[12pt]
\dfrac{M^2}{1-M^2} & -\dfrac{1}{1-M^2} & -\dfrac{\gamma M^2}{2(1-M^2)} & -\dfrac{(\gamma+1)M^2}{1-M^2} & \dfrac{1}{1-M^2} & 0 \\[12pt]
\dfrac{\gamma M^2}{1-M^2} & -\dfrac{\gamma M^2}{1-M^2} & -\dfrac{\gamma M^2(1+(\gamma-1)M^2)}{2(1-M^2)} & -\dfrac{2\gamma M^2\left(1+\frac{\gamma-1}{2}M^2\right)}{1-M^2} & \dfrac{\gamma M^2}{1-M^2} & 0 \\[12pt]
\dfrac{1}{1+\gamma M^2} & 0 & -\dfrac{\gamma M^2}{2(1+\gamma M^2)} & 0 & 0 & 0 \\[12pt]
0 & 1 & \dfrac{(\gamma-1)M^2}{2} & (\gamma-1)M^2 & 0 & 0
\end{bmatrix}
\begin{bmatrix} \dfrac{dA}{A} \\[6pt] \dfrac{dQ-dW_x+dH}{C_pT} \\[6pt] \dfrac{4f}{D}dx-2\dfrac{u_g}{u}\dfrac{d\dot m}{\dot m} \\[6pt] \dfrac{d\dot m}{\dot m} \\[6pt] \dfrac{dW}{W} \\[6pt] \dfrac{d\gamma}{\gamma} \end{bmatrix}
$$

Bibliography

[1] C. Aguilera. *Effect of Fin-Guided Fuel Injection on Supersonic Mixing and Combustion*. PhD dissertation, University of Maryland College Park, 2014.

[2] M. Deepu, S.S. Gokhale, and S. Jayaraj. Numerical modelling of scramjet combustor. *Defence Science Journal*, 57(4):367-379, 2007.

[3] D.B. Le, C.P. Goyne, R.H. Krauss, and J.C. McDaniel. Experimental study of a dual-mode scramjet isolator. *Journal of Propulsion and Power*, 24(5):1050-1057, 2008.

[4] W.H. Heiser and D.T. Pratt. *Hypersonic Airbreathing Propulsion*. American Institute of Aeronautics and Astronautics, Inc., Washington, DC, 1994.

[5] M.L. Fotia and J.F. Driscoll. Assessment of isolator pseudo-shocks created by combustion with heated flow. 17th *AIAA International Space Planes and Hypersonic Systems and Technologies Conference*, (AIAA Paper 2011-2222), April 2011.

[6] M.L. Fotia and J.F. Driscoll. Ram-scram transition and flame/shock-train interactions in a model scramjet experiment. *Journal of Propulsion and Power*, 29(1):261-273, 2013.

[7] E.T. Curran. Scramjet engines: the first forty years. *Journal of Propulsion and Power*, 17(6):1138-1148, 2001.

[8] C.P. Goyne, C.G. Rodriguez, R.H. Krauss, J.C. McDaniel, and C.R. McClinton. Experimental and numerical study of a dual-mode scramjet combustor. *Journal of Propulsion and Power*, 22(3), 2006.

[9] M.K. Smart. Scramjet isolators. *AVT-185 RTO AVT/VKI Lecture Series*, von Karman Institute, Belgium, September 2010.

[10] J.S. Geerts and K.H. Yu. Experimental characterization of isolator shock train propagation. *18ᵗʰ AIAA International Space Planes and Hypersonic Systems and Technologies Conference*, (AIAA Paper 2012-5891), September 2012.

[11] K. Matsuo, Y. Miyazato, and H.D. Kim. Shock train and pseudo-shock phenomena in internal gas flows. *Progress in Aerospace Sciences,* 35:33-100, 1999.

[12] B. Morgan, K. Duraisamy, and S.K. Lele. Large-eddy simulation of a normal shock train in a constant-area isolator. *AIAA Journal*, 52(3), 2014.

[13] L. Sun, H. Sugiyama, K. Mizobata, R. Minato, and A. Tojo. Numerical and experimental investigations on Mach 2 and 4 pseudo-shock waves in a square duct. *Trans. Japan Soc. Aero. Space Sci.,* 47(156), 2004.

[14] H.J. Tan, S. Sun, and H.X. Huang. Behavior of shock trains in a hypersonic inlet/isolator model with complex background waves. *Exp. Fluids*, 53:1647-1661, 2012.

[15] J.A. Fulton, J.R. Edwards, H.A. Hassan, J.C. McDaniel, C.P. Goyne, R.D. Rockwell, A.D. Cutler, C.T. Johansen, and P.M. Danehy. Large-eddy/Reynolds-averaged navier-stokes simulations of reactive flow in dual-mode scramjet combustor. *Journal of Propulsion and Power*, 30(3):558-575, 2014.

[16] J.Y. Choi, F. Ma, and V. Yang. Combustion oscillations in a scramjet engine combustor with transverse fuel injection. *Proceedings of the Combustion Institute,* 30:2851-2858, 2005.

86

[17]   M. Berglund and C. Fureby. LES of supersonic combustion in a scramjet engine model. *Proceedings of the Combustion Institute*, 31:2497-2504, 2007.

[18]   C. Segal. *The Scramjet Engine: Processes and Characteristics*. Cambridge University Press, 2009.

[19]   C.F. Delale and M.E.H. van Dongen. Thermal choking in two-dimensional expansion flows. *Z. angew. Math. Phys.*, 49:515-537, 1998.

[20]   K.H. Yu, K.J. Wilson, and K.C. Schadow. Effect of flame-holding cavities on supersonic-combustion performance. *Journal of Propulsion and Power*, 17(6):1287-1295, 2001.

[21]   D.J. Micka and J.F. Driscoll. Combustion characteristics of a dual-mode scramjet combustor with cavity flameholder. *Proceedings of the Combustion Institute*, 32:2397-2404, 2009.

[22]   T. Mathur, M. Gruber, K. Jackson, J. Donbar, W. Donaldson, T. Jackson, and F. Billig. Supersonic combustion experiments with a cavity-based fuel injector. *Journal of Propulsion and Power*, 17(6):1305-1312, 2001.

[23]   H. Wang, M. Sun, H. Wu, and Z. Wang. Characteristics of oscillations in supersonic open cavity flows. *Flow, Turbulence Combustion*, 90:121-142, 2013.

[24]   COMSOL Company Website. *About Us* page. www.comsol.com/company, 2014.

[25]   *COMSOL Multiphysics Reference Manual*. COMSOL documentation, COMSOL, version 4.4, 2013.

[26]   *CFD Module User's Guide*. COMSOL documentation, COMSOL, version 4.4, 2013.

87

[27]   J.D. Anderson. *Modern Compressible Flow with Historical Perspective*. McGraw-Hill, Inc., 3 edition, 2003.

[28]   D.C. Wilcox. *Turbulence Modeling for CFD*. DCW Industries, 2 edition, 1998.

[29] P.R. Spalart and S.R. Allmaras. A one-equation turbulence model for aerodynamic flows. *30th Aerospace Sciences Meeting & Exhibit*, (AIAA Paper 92-0439), January 1992.

[30] COMSOL Company Website. *Solutions to Linear Systems of Equations: Direct and Iterative Solvers.* www.comsol.com/blogs/solutions-linear-systems-equations-direct-iterative-solvers/, 2013.

[31] M.R. Hesteness and E. Stiefel. Methods of Conjugate Gradients for Solving Linear Systems. *Journal of Research at the National Bureau of Standards*, 49(6):409-436, 1952.

[32] F. Schlegel. CFD II Minicourse – Turbulent and High Mach Number Flow. *2014 COMSOL Conference Boston Minicourse,* October 2014.

[33] *Transonic Flow in a Nozzle*. COMSOL Model Library Tutorial, COMSOL, version 4.3a, 2012.

[34]   *Introduction to CFD Module.* COMSOL documentation, COMSOL, version 4.4, 2013.

[35]   *Transonic Flow in a Sajben Diffuser*. COMSOL Model Library Tutorial, COMSOL, version 4.4, 2013.

[36]   J. Geerts. PhD candidate, University of Maryland College Park, 2014.

[37] A.H. Shapiro. *The Dynamics and Thermodynamics of Compressible Fluid Flow, Volume I,* The Ronald Press Company, 1953.

[38] H.W. Leipmann and A. Roshko. *Elements of Gasdynamics*. Dover Publications, Inc., 2001.

[39] *MIL-HDBK-5H: Metallic Materials and Elements for Aerospace Vehicle Structures.* Department of Defense Military Handbook, edition 5H, 1998.

[40] P. Hill and C. Peterson. *Mechanics and Thermodynamics of Propulsion.* Addison-Wesley Publishing Company, Inc., 2 edition, 1992.